ASE-3851

NASA CR-145036

FINAL REPORT

# DEVELOPMENT AND EVALUATION OF A HADAMARD TRANSFORM IMAGING SPECTROMETER AND A HADAMARD TRANSFORM THERMAL IMAGER

By Martin Harwit, Roderick Swift, Richard Wattson, John Decker and Ralph Paganetti



Prepared under Contract No. NAS1-12690 by

American Science and Engineering, Inc.
955 Massachusetts Avenue
Cambridge, Massachusetts 02139

for

NASA
National Aeronautics and Space Administration

## TABLE OF CONTENTS

CONTENTS (Continued)

## ILLUSTRATIONS

## ILLUSTRATIONS (Continued)

## ACKNOWLEDGEMENTS

This work was sponsored by the National Aeronautics and Space Administration, Langley Research Center in Hampton, Virginia under the direction of Mr. Daniel J. Jobson, Technical Representative.

# DEVELOPMENT AND EVALUATION OF A HADAMARD TRANSFORM IMAGING SPECTROMETER AND A HADAMARD TRANSFORM THERMAL IMAGER

By Martin Harwit, * Roderick Swift, Richard Wattson, John Decker* and Ralph Paganetti

SUMMARY

A spectrometric imager and a thermal imager, which achieve multiplexing by the use of binary optical encoding masks, have been built and tested. The masks are based on orthogonal, pseudo-random digital codes derived from Hadamard matrices. Spatial and/or spectral data is obtained in the form of a Hadamard transform of the spatial and/or spectral scene; computer algorithms are then used to decode the data and reconstruct images of the original scene. The hardware, algorithms and processing/display facility are described. A number of spatial and spatial/spectral images, obtained in the laboratory, are presented.

The achievement of a signal-to-noise improvement due to the signal multiplexing was also demonstrated during the test program. These measurements and calculations are reported, as is an analysis of the results which indicates both the situations for which the multiplex advantage may be gained, and the limitations of the technique. A number of potential applications of the spectrometric imager are discussed.

---

*Spectral Imaging, Inc.
Dr. Harwit is Principal Investigator
Dr. John Decker is one of the Co-Investigators

## 1.0 INTRODUCTION

In the late 1940's Marcel Golay[1] wrote a series of remarkable papers in which he showed that a beam of radiation passing through a dispersing spectrometer could be modulated by passage through partially opaque mask patterns placed at the entrance and/or exit apertures; and the modulated beam could then be used to obtain spectral information at a far higher rate or with a larger signal-to-noise ratio than available from a conventional dispersing instrument.

These papers were far ahead of their time, in that Golay realized the importance of orthogonal binary digital codes more than a decade before digital computers had proven their real worth, and more than two decades before small digital computers were to become standard equipment in many laboratories.

Golay showed that a "multiplex advantage" could be gained in his method because different spectral elements of the beam could be made to impinge on the detector for as much as one half of the time available for making the measurements, while a conventional scanning spectrometer allowed each of the N spectral elements to impinge on the detector for only 1/N of the available time. The signal-to-noise ratio could therefore be improved by a factor of order $(N/2)^{1/2}$.

Some twenty years after Golay's work, many of the essential features of his instrumentation were rediscovered by Ibbett, Aspinall and Grainger[2] and by Decker and Harwit[3]. In the same year, 1968, Gottlieb[4] also showed that digital multiplexing by means of opaque masks could be useful in image analysis. In that case the optical instrument was used to isolate individual spatial rather than spectral elements in a beam of radiation, but the mathematical treatment of the multiplexing scheme remained essentially unchanged.

Gottlieb noted two important points. First, there exist cyclic codes intimately related to orthogonal binary digital codes; second these codes can be folded into a two-dimensional array, much as the one-dimensional lines of written words are folded into a two-dimensional array of writing on this page. The advantage of folding is that one-dimensional codes are mathematically far better understood than their two-dimensional analogues. The advantage of cyclic codes is that one can construct a large single mask, overlapping portions of which form essentially orthogonal arrays. Mask production costs are therefore greatly lowered, and the multiplexing method immediately becomes economically attractive. Golay's mask patterns were not cyclic and would have been exorbitantly expensive in any apparatus dealing with a large number of discrete elements.

Sloane et al[5] examined various codes and found that the Reed-Muller codes used by Gottlieb would also be well suited for spectrometry. These codes were used in the first full scale realization of such a spectrometer. Decker[6] constructed a 255-element spectrometer based on these codes and showed quantitatively that the theoretical advantages in signal-to-noise ratio can actually be realized. Since the Reed-Muller codes are related to Hadamard matrices -- orthogonal binary digital arrays -- this type of instrument has been called a Hadamard transform spectrometer. Sloane et al had already shown the degree of degradation to be expected from the use of Reed-Muller codes relative to Hadamard encoding, and in 1970 Nelson and Fredman[7] showed that the Hadamard codes set an absolute standard of perfection for binary digital encoding. Other binary digital codes may exist, but they cannot be better.

In 1970 Harwit et al[8] also showed that a dispersing spectrometer can be encoded at both the entrance and exit aperture to increase the optical throughput of a grating spectrometer when light from a

diffuse extended source is imaged on the instrument's entrance aperture. Such an instrument has now been constructed[9]. Making use of the optical system needed for this purpose, Phillips and Harwit[10] were then able to show that an alternate reduction of the spectral data obtained could yield several different spectra corresponding to different spatial strips or adjacent spectrometer slit positions in the spectrometer entrance focal plane.

An extension of these techniques has combined two-dimensional spatial encoding with one-dimensional spectral encoding, in an instrument Harwit[11] has named a "spectrometric imager". In 1972 a pilot model of this invention was built[12] to show that the technique could be realized in practice.

We now report on the results of a program which had as its primary objectives: (1) the development of a full scale spectrometric imager for laboratory testing, (2) development of the associated computer software and display capabilities, and (3) evaluation of the technique for future flight experiments requiring high spatial, spectral and temporal resolution. The approach ot these goals was through the parallel implementation of the data processing facility and a breadboard version of a spectrometric imager, which allowed testing and software development to proceed while an engineering model instrument, capable of use aboard a NASA aircraft, was designed and built. From the start, it was recognized that the apparatus would not be the best design for any specific application. Instead, the techniques would be developed, with the understanding that the results could readily be extrapolated to assess the potential applications. For this reason, maximum use was made of commercially available instrumentation so that the main objectives could be approached most expeditiously.

For some applications spectral data is either irrelevant (e.g., thermal imaging), or is needed for only a few spectral bands. An extension of the above program, with similar objectives, provided for the evaluation of the Hadamard transform encoding technique for spatial imaging alone. This was made possible because the spatial encoding is accomplished by a separate subassembly, usable as a focal plane device in itself.

In this report, we refer to the spectrometric imager as a Hadamard transform imaging spectrometer (HADIS). Its imaging only counterpart is called a Hadamard transform imager (HADIM). For both instruments we discuss the opto-mechanical design, the electronic requirements, the computer reduction of data and the different modes of data display made available by our computer programs. The results of laboratory tests for both spatial and spatial/spectral imaging is presented. We analyze the advantages to be gained in signal-to-noise ratio under different modes of operation, discuss the limitations of the technique, and finally discuss some of the potential future applications.

## 2.0 HADAMARD TRANSFORM IMAGING SPECTROMETER

A block diagram of the Hadamard transform imaging spectrometer (HADIS) is shown in Figure 1. The spatial/spectral scene is focused onto a field stop at the entrance focal plane of a dispersion spectrograph by an objective lens or telescope. A two-dimensional, binary optical mask, based on cyclic Hadamard codes, is scanned across the field stop, thus transmitting a time-varying light intensity that contains information about all spatial resolution elements in terms of the sequence of mask patterns. This radiation is then dispersed and focused as a spectrum at the exit focal plane of the spectrograph. A one-dimensional Hadamard mask is placed across the spectrum and stepped one element of its cycle for each complete cycle of the spatial code. This, too, produces modulation containing spectral information.

Having been encoded in the above manner, the radiation from the spatial/spectral scene is de-dispersed and condensed onto a suitable detector. The time-varying signal which is thus produced represents the Hadamard transform of the original spatial/spectral scene, which may be reconstructed by the use of computer algorithms similar to the well-known fast Fourier transform (FFT) algorithms. Multiplexing is achieved by virtue of the fact that each spatial/spectral resolution element is observed many times during the entire scan (rather than only once, as it would be in a single detector scanning system having the same frame time); in some situations this may lead to improvements in signal-to-noise (S/N) in the reconstructed image. This is analyzed in more detail in Section 7.

An illustration of the HADIS is shown in Figure 2, as is a photograph of the instrument from the opposite side, showing the spatial encoding assembly and objective lens. The electronics are con-

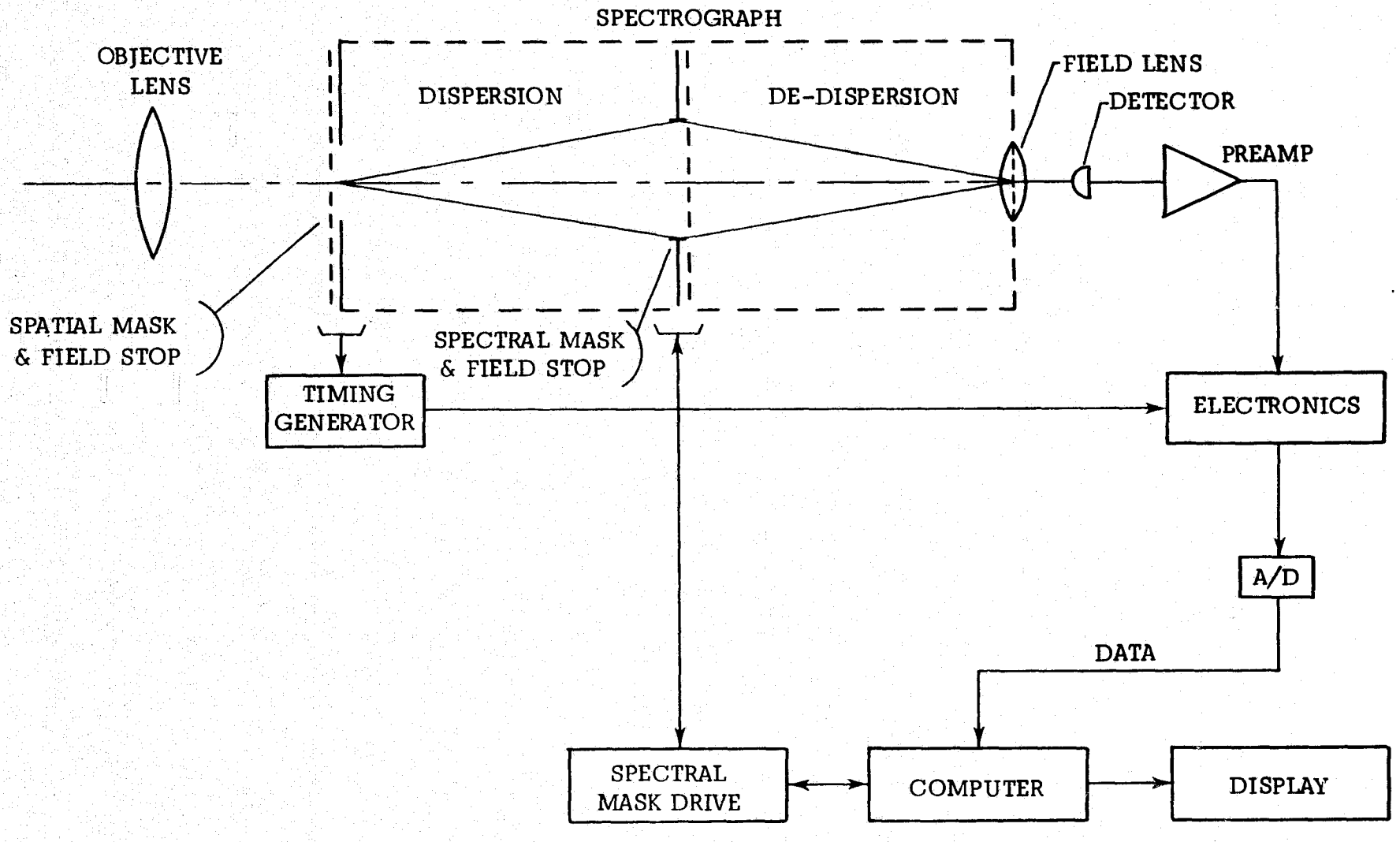


Figure 1. Block Diagram of the Hadamard Transform Imaging Spectrometer (HADIS)

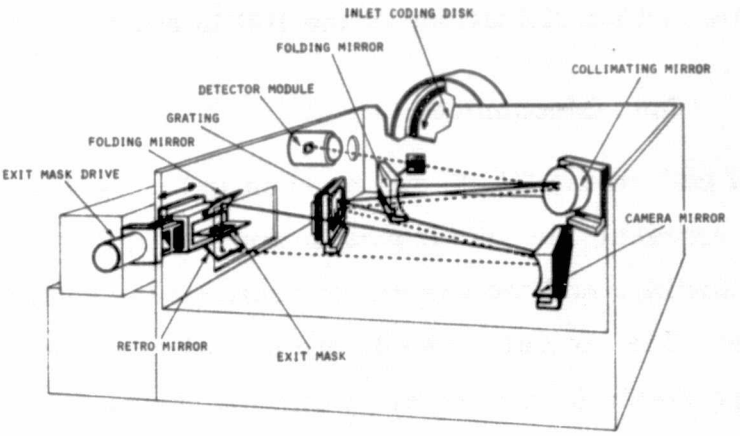


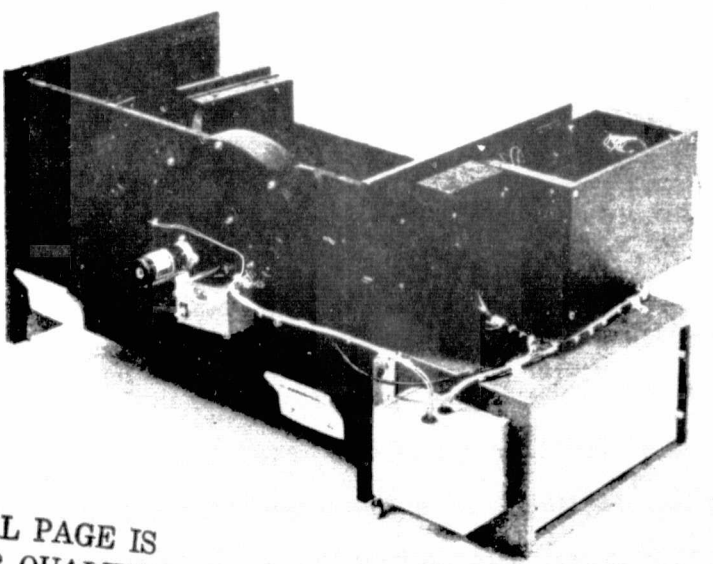



CY-079

Figure 2. Schematic Drawing and Photograph of the HADIS

tained in the large chassis below the exit mask drive assembly. The spectrograph optics are normally enclosed by a cover. The design goals and specifications of the HADIS are given in Table 1.

## 2.1 Opto-Mechanical Layout

The optical path of the HADIS can be seen in Figure 2, where the solid line represents the incident radiation, up to the point of spectral encoding, and the dashed line follows the return beam to the detector. The optical elements are an objective lens, the spectrograph optics (including the grating), mirrors to retro-reflect the encoded spectrum, and field optics for the detector.

The object, or scene, is focused by the objective lens onto a portion of the spatial encoding mask determined by a field stop. Light passing through the field stop and mask is collimated and directed onto the grating, where it is dispersed. The camera mirror causes the spectrum to be brought to a focus at the exit mask, where images of the entrance mask in different wavelengths result. The reason a spectrograph (rather than a spectrometer) is required is because of the need for an extended focal plane to image an extended spectrum. A portion of the spectrum is transmitted by a spectral field stop located at the focal plane.

In order to condense the encoded radiation onto the smallest possible detector, a reverse-pass off the grating is used to de-disperse the spectrum. The final image is separated from the input image by displacing the spatial field stop below the horizontal centerline of the spectrograph, displacing the detector upwards, and using two folding mirrors to separate the incident and return beams at the exit focal plane. Note that the image of the entrance plane at the exit plane of the spectrograph is inverted. The shorter wavelengths are focused at the end of the spectrum nearest the grating, longer wavelengths at the more remote end.

## Table 1: HADIS Design Specification

| | |
|---|---|
| Wavelength range: | 8-14 μm |
| Spectral resolution: | Grating dependent (see Section 2.1.2) |
| Spectral channels: | 63 |
| Field of view: | $8.88^{o} \times 9.45^{o}$ |
| Spatial resolution: | .005 radians |
| Spatial resolution elements: | 1023 (31 x 33) |
| Detectors: | (a) PbSe (See Table 2, Section 2.3.1) |
| | (b) Pyroelectric (See Table 3, Section 2.3.2) |

| | PbSe | Pyroelectric |
|---|---|---|
| Scanning drive speed: | 720 RPM | 20 RPM |
| Spatial frame time: | 27 msec | ~ 1 sec |
| Spatial/Spectral frame time: | 2.6 sec | ~ 95 sec |

In designing the HADIS, it was first necessary to select a spectrograph having performance compatible with the design goals of the program. The design of the encoding masks and drives, objective and detector optics, and retro-reflection system would follow. These items are discussed in the appropriate order in the following sections.

### 2.1.1 Spectrograph

As with other optical systems, the total light energy collected by the HADIS (i.e., its signal) is proportional to the area of its entrance pupil, which is the image of its aperture stop produced by the preceeding optical elements. Economics dictate that the limiting aperture of a spectrograph is generally the diffraction grating itself. Similarly, to collect all that energy, the detector must fill the exit pupil of the optical system which is the image of the aperture stop produced by the optical elements which follow. Most detectors, particularly in the infrared, have inherent noise generation that scales only as the square-root of their area. Consequently, there is something to be gained in S/N by using the largest possible optical system (including the focal length of the spectrograph), and for a given focal length, using the fastest possible spectrograph optics.

In keeping with the decision to use standard components to the maximum extent, a search was conducted to locate the fastest commercially available spectrographs. Furthermore, it was decided that a 1/2 meter (focal length) spectrograph was the largest reasonable size to use, and that its optics should be of the Czerny-Turner type because of its inherently good image qualities for off-axis radiation.[13-17] Several candidate instruments were found that had approximately f/8 optical systems; it is not customary to build faster high-resolution spectrographs

because of the difficulty of minimizing aberrations over an extended focal plane.

Had a special spectrograph been designed, say a 1 meter, f/2 system for example, it is interesting to note that a potential gain of a factor of 8 in S/N might have been anticipated. It is unlikely that this could be achieved, however, due to the often overlooked fact that large detectors (64 times the area in this case) rarely have the same noise performance, or D*, of their smaller counterparts.

The instrument selected was a 1/2 meter Czerny-Turner spectrograph with approximately f/7 optics, a 100mm focal plane, and with mirrors large enough to allow the use of 2cm high slits without vignetting or excessive aberrations. It utilized standard gratings of ruled area 64mm x 64mm, and had a $45^{\circ}$ folding mirror in the optical path (see Figure 2), which was easily modified to allow physical separation of the incident and return images. Ray tracing showed that only the central 4mm of the entrance slit height needed to be avoided in order to completely separate the two images without vignetting. Since spectrograph optics are not corrected for astigmatism in the direction perpendicular to the plane of dispersion, it was also decided to avoid the last 2mm as well, leaving a height of $\approx$ 6mm for the off-center entrance mask field stop.

It is a property of the spectrograph's optical system, that astigmatism is minimized by the use of slightly curved entrance and exit slits. This curvature was found to be on the order of 100mm radius for our spectrograph, and was used as the average radius of a disc containing the spatial encoding mask. The code is then cycled through its entire set of mask configurations by simple rotation of the disc.

## 2.1.2 Encoding Mask Design

It was a design goal of the program to use a 1023 element Hadamard code, factored into a 31 x 33 array for spatial encoding, and a 63 element linear Hadamard code for spectral encoding. The decoding process is simplified if there is a one-to-one correspondence between the vertical columns of the spatial array and the vertical slits of the spectral mask. Such a correspondence means that the relative sizes of the masks must be adjusted, accounting for the optical magnification of the spectrograph, so that (for any given wavelength) the 31 entrance mask columns are imaged onto 31 slits of the exit mask.

Anamorphic Magnification: Analysis of the optical system of the spectrograph, where the grating is treated only as a reflective element, showed the entrance-to-exit focal plane magnification to be 0.960. However, there is an anamorphic magnification[18] as a result of the dispersion of the grating. It is given by:

$$\frac{d\beta}{d\alpha} = - \frac{\cos\alpha}{\cos\beta} \qquad (1)$$

where $\alpha$ is the angle of incidence and $\beta$ the angle of diffraction relative to the grating normal, and must be applied as a correction in the direction of dispersion only. As shown by the first order grating equation:

$$\lambda = a \ (\sin\alpha + \sin\beta) \qquad (2)$$

both $\alpha$ and $\beta$ depend on the grating ruling, a, and the orientation of the grating required to image a wavelength $\lambda$ in the spectrograph's focal plane; also, $\beta$ varies across the focal plane. The anamorphic effect was calculated, based on the optical layout of the spectrograph, and verified by experiment. A mean value of 1.075 was used, based on a 20 groove/mm grating set for a central wavelength

of 15μm. (It was our original intent to design the HADIS for use from 6μm to 25μm).

Exit Mask Configuration: We previously determined that a height of about 6mm was available for the spatial field at the entrance plane. Since this field is approximately square, and contains 31 elements in the horizontal direction, each element must be $\simeq$ 0.2mm wide. Accounting for the magnification of the spectrograph, both linear and anamorphic, the exit mask slits must also have about this dimension. However, as it is necessary to position the exit mask with precision, the actual dimension had to be made compatible with available lead-screw/stepper motor combinations. The best match was obtained by the use of a 200 step per revolution motor coupled to a 2.54mm (0.1") pitch lead-screw. By incrementing 14 steps, the advance is 0.1778mm (0.007"). The motor can be driven at 2000 steps/sec. Only 15msec is required to position the spectral mask assembly between spatial scans, where an allowance is made for settling time.

The elemental size of 0.1778mm (0.007") leads to a total encoded length of 63 x 0.1778mm = 11.2mm (only a small portion of the full 100mm focal plane). The encoding mask itself, in order to cycle through the entire code, has to have 62 additional positions. Its length, is then 22.225mm. The heights of the mask slits were made 40 times their width in order to allow plenty of room for transmission of the astigmatic image of the entrance mask columns. The exit mask and field stop are shown in Figure 3. The slits are curved to match the curvature of the entrance encoding disc, and are assymetric to account for the offset of the image from the optical axis of the spectrograph.

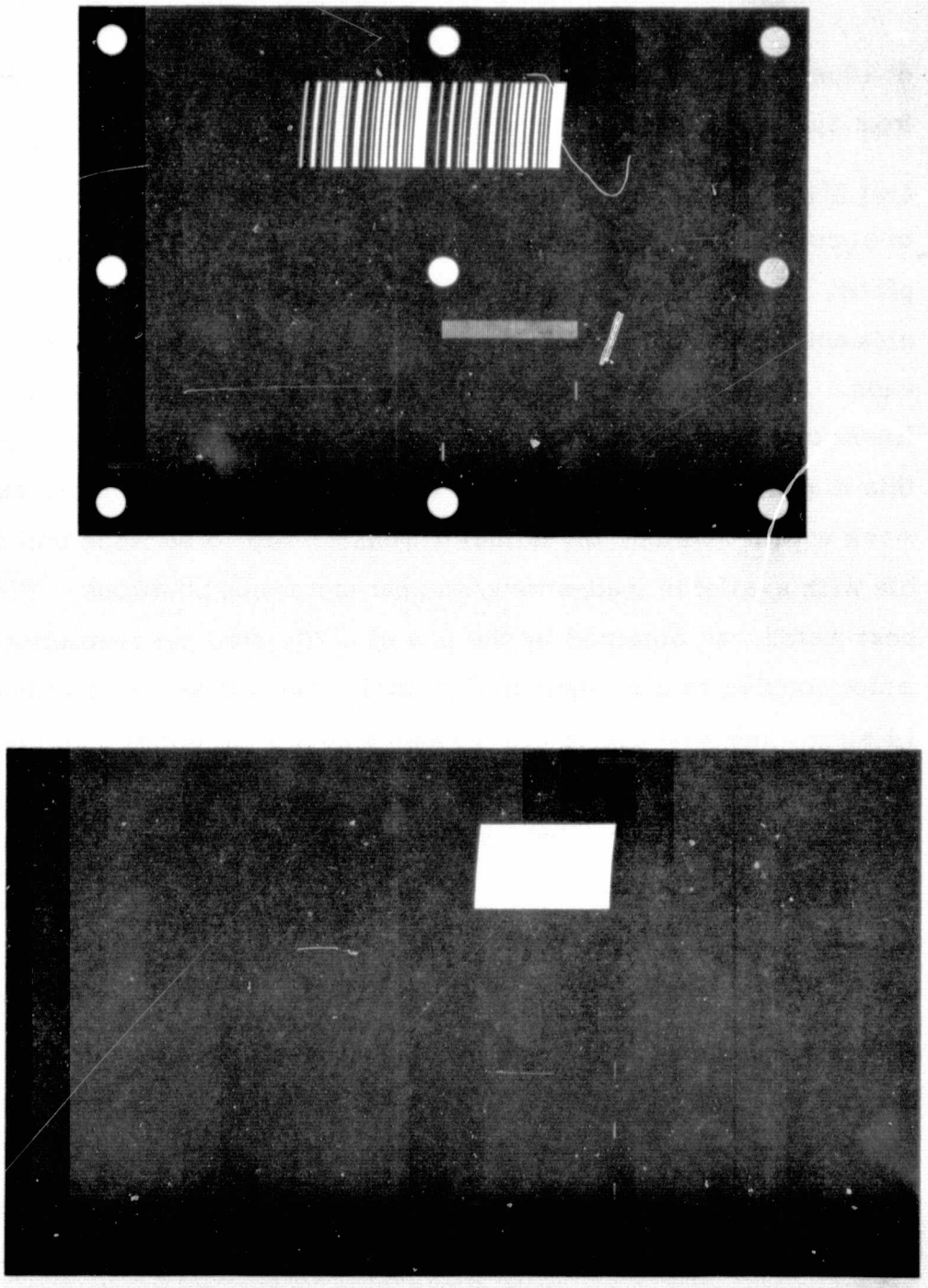

Figure 3. HADIS Exit (Spectral) Mask and Field Stop

The mask code was determined by the method described in Section 4, and was used by the manufacturer of the masks to program a computer controlled ruling engine which generated the required "artwork". The masks themselves are fabricated in a nickel foil supported on a copper substrate.

Spectral Resolution: The spectral resolution depends, of course, on the dispersion of the diffraction grating, the actual dimensions of the spectrograph, and the size of the encoding slits. It can be closely estimated by extrapolation from the nominal dispersion (given by the manufacturer of the spectrograph): 16Å (angstroms)/mm for a 1200 groove/mm grating. If we assume a 20 groove/mm grating, we have a resolution given by:

$$R_{20} \simeq \frac{16\text{Å}}{\text{mm}} \times \frac{10^{-4}\,\mu\text{m}}{\text{Å}} \times \frac{1200}{20} \times 0.1778\text{mm} \simeq .017\mu\text{m} \qquad (3)$$

Ray tracing of the spectrograph showed that it is impractical to use a grating blaze angle smaller than $\simeq 0^{\circ}45'$. The zero-order (undispersed) radiation enters the spectral field stop for smaller blaze angles. For example, this angle corresponds to a 3 groove/mm grating blazed for 8μm, or a 7.2727 groove/mm grating blazed for 3.6μm. The corresponding resolutions are given by:

$$R_3\,(8\mu\text{m}) \simeq 0.11\mu\text{m} \qquad (4)$$

$$R_{7.27}\,(3.6\mu\text{m}) \simeq 0.047\mu\text{m} \qquad (5)$$

The actual resolving power was determined by experiment (7.2727 groove/mm grating) to be about 10% less than given by the above values.

Entrance Mask Configurations: The size of the resolution elements for the spatial encoding mask was determined from the exit mask element size, by applying the linear magnification 0.960

and mean anamorphic magnification 1.075 of the spectrograph:

$$\text{element size} = \frac{0.1778\text{mm}}{(.960)\,(1.075)} = .1723\text{mm} \qquad (6)$$

Since the actual mask was fabricated with polar coordinates, the radial increments, of which there are 31, were made to have the above value, and the angular increments were spaced at $0^{\circ}6'15''$ of arc, which corresponds very closely to the above size at the mean radius 94.742mm (3.73") of the 16th radial element. The field stop was made to span 31 radial x 33 angular elements of the mask.

Since the spatial code was to be cycled through its 1023 independent configurations by the rotation of a disc, it was necessary to have at least 1022 angular positions in addition to the 33 required to fill the spatial field stop at any given time. The total encoded arc was then required to be at least $109^{\circ}53'45''$. In fact, an extra 33 positions were added at the end (so the same configuration would appear both at the beginning and at the end of a scan for comparison), giving a total mask arc of $113^{\circ}20'00''$. There would have been room for three such masks on the periphery of the scanning disc; however, only two masks were used, with $66^{\circ}40'$ between them, in order to allow sufficient time for the taking of dark samples and stepping the spectral mask. The entrance mask and field stop are shown in Figure 4. As mentioned before, the average radius of curvature of the mask was picked to match the optimum slit curvature for the spectrograph. Code generation was as described for the case of the spectral mask. Note that each radial increment of the mask contains the complete 1023 element cyclic code, but each radius differs in phase from its neighbors by an increment of 33 code elements.

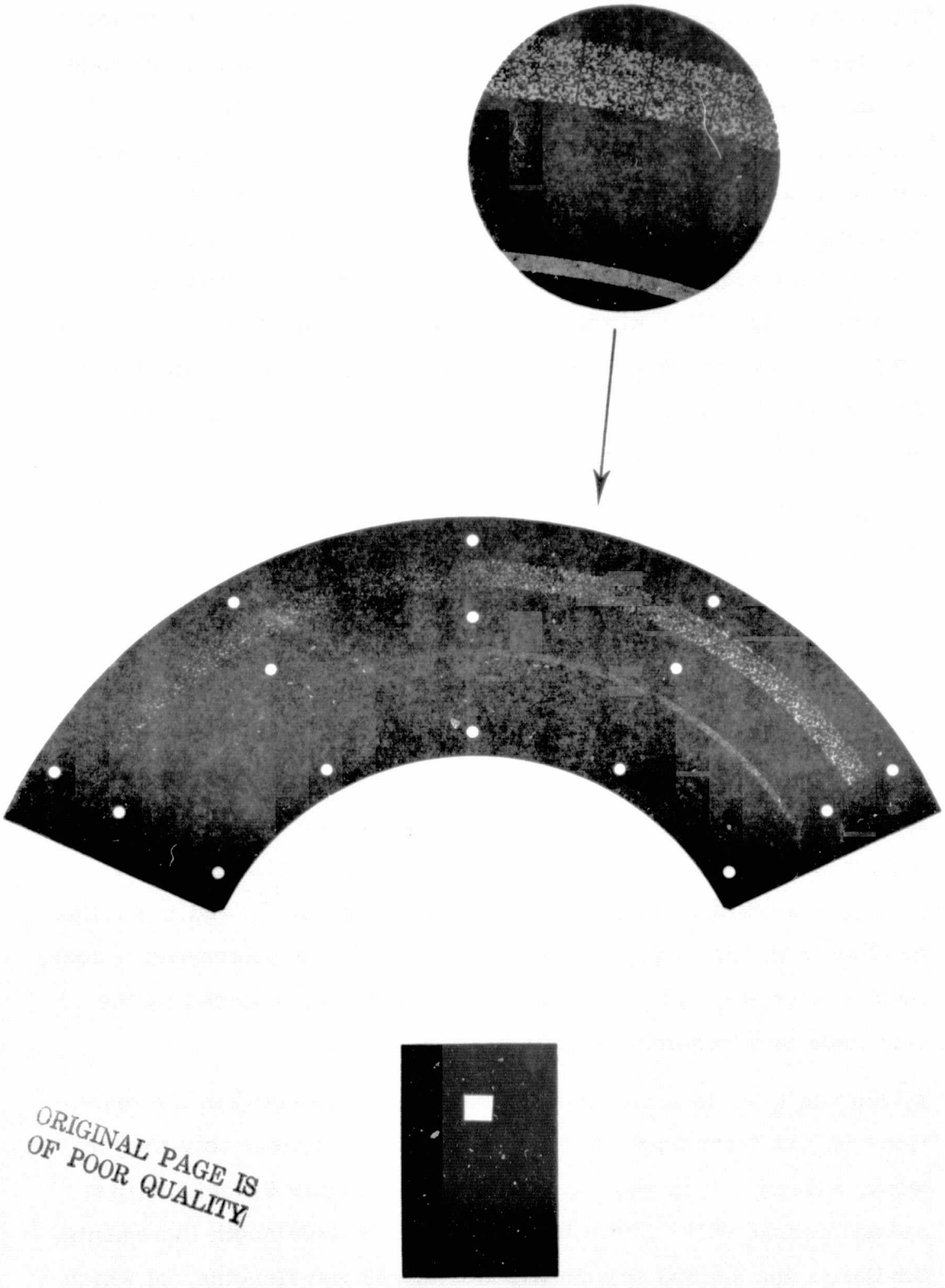



Figure 4. HADIS Entrance (Spatial) Mask and Field Stop

The entrance mask presented a new problem in fabrication: it was not desired to use a solid substrate, and the two-dimensional code could not be self-supporting. Consequently, it was necessary to superimpose it on a spiderweblike grid having similar angular and radial element spacings. Calculations showed that grid elements of width 0.025mm (0.001") would withstand the dynamic loads of the rotating mask elements. The transmission of this grid is approximately 65%. Artwork for the spatial mask and the supporting grid was generated independently, and combined into a single master for the actual fabrication process. The spatial masks are also fabricated in this nickel supported by a copper backing.

Spatial/Spectral Overlap: The nature of a spectrograph is such that the entrance focal plane is imaged onto the spectral focal plane, the images being shifted only according to wavelength. Consequently, the image of the extended entrance mask for any given wavelength will lie over a number of adjacent spectral mask locations. Similarly, the image for a slightly different wavelength (e.g., one corresponding to one spectral resolution element difference) will be imaged so that it overlaps the first image. This aspect of simultaneous encoding at both entrance and exit focal planes of a spectrograph was discussed by Harwit[12], and is easily handled in the decoding process, to yield true monochromatic images, by a "reassembly" of the spatial/spectral images obtained by the fast Hadamard transform (FHT) algorithm.

As long as there is a one-to-one correspondence between the resolution element sizes at the two focal planes, the reassembly routine works exactly. It is easy to visualize (see Figure 5) that the first spatial column will contain information at 63 wavelength increments. Similarly, the second column will contain 63 wavelengths, of which 62 are common to the first column, and so on. Some information

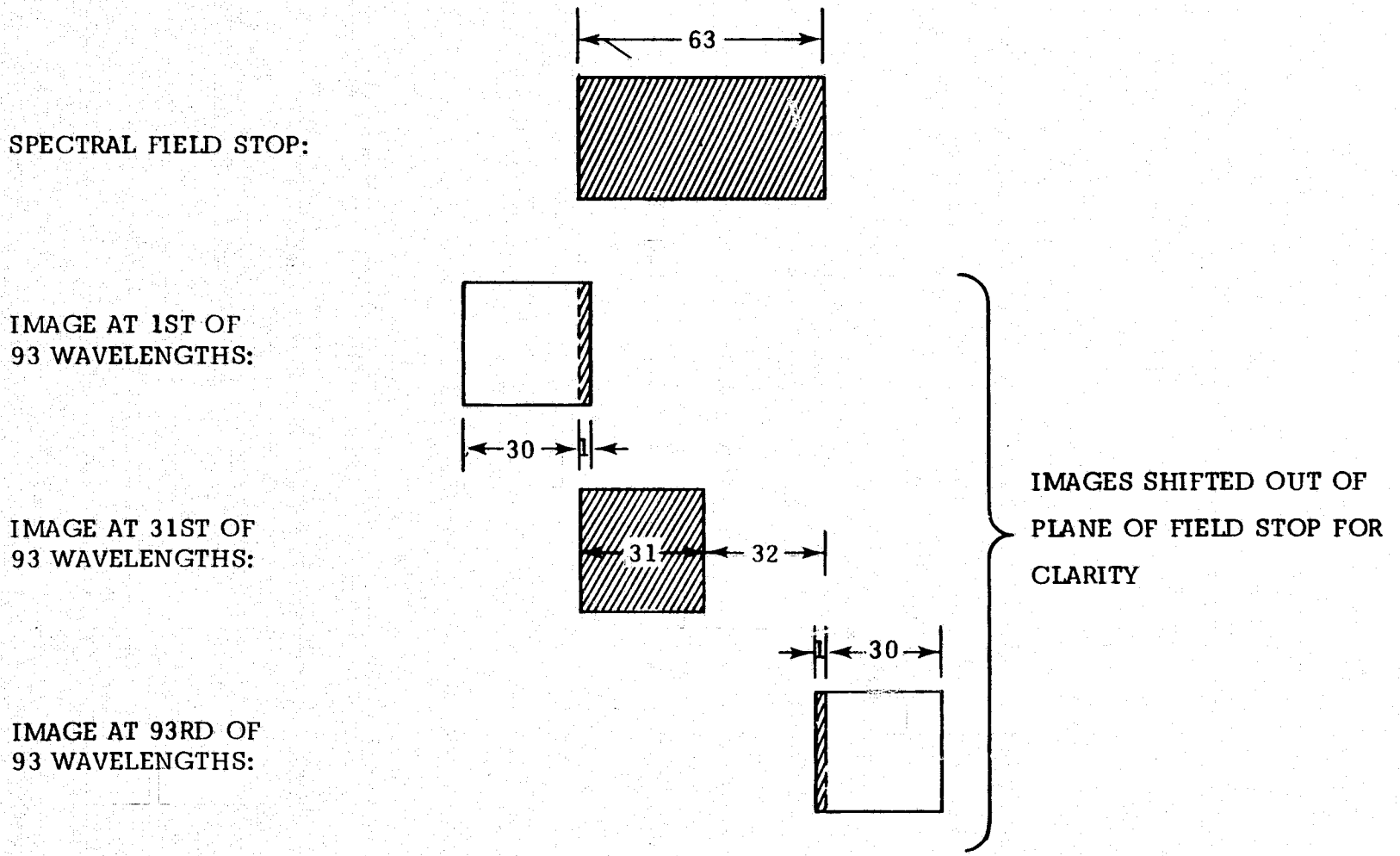


Figure 5. Conceptual Illustration of the Overlap of Spatial/Spectral Information

is obtained at 63 + 30 = 93 wavelengths. The first 30 wavelengths will correspond to monochromatic images having a width less than the full 31 columns; this is also true for the last 30 wavelengths. There will be 33 "complete" monochromatic images for the 33 middle wavelengths. The grating alignment and computer software has been set up to produce the correct images and properly identify their wavelengths.

The anamorphic effect means that there cannot truly be a one-to-one correspondence between masks at the two focal planes. Its effect on the reassembly algorithm has not been analyzed, but we believe that images reconstructed without correcting the algorithms are not exactly monochromatic, they retain a slight variation in wavelength from one edge of the field to the other. No serious effects are observed for the case of a 7.2727 groove/mm grating set for a central wavelength of 2.5$\mu$m, for which the anamorphic magnification is estimated to be $\simeq$ 1.01 instead of the design value 1.075.

### 2.1.3 Objective Lens

The HADIS was designed to have a nominal spatial resolution of 5 milliradians, covering a $9.45^{\circ}$ x $8.88^{\circ}$ field in 33 x 31 elements. (In fact, the field is slightly wedge-shaped because of the radial symmetry of the encoding pattern.) The resolution element dimension of 0.1723mm then requires an objective lens focal length of 34mm.

It has been mentioned that the entrance pupil of the HADIS is the image of the aperture stop (the diffraction grating), as formed by all preceeding optical elements -- in this case, the collimating mirror and the objective lens. The size of this entrance pupil was calculated based on the optical layout of the spectrograph, a 34mm focal length objective lens, and an effective grating size of 64mm x 64mm. The entrance pupil lies 34.3mm in front of the objective lens, and has dimensions 4.35mm x 4.35mm. Note that the small size of the entrance pupil is primarily due to the small grating (aperture stop) required in a reasonably sized instrument of high f/number (f/7).

Because it is located some distance behind the entrance pupil, and has an extended field of view, it was necessary to provide an objective lens diameter substantially greater than what would have been required for an f/7 lens. Vignetting of off-axis radiation is eliminated only by making its diameter 14.5mm.

The lens was fabricated from KRS-5 (thallium bromoiodide) with a design wavelength of 11.5$\mu$m, conjugate at infinity. The material has an index of refraction of about 2.38 near 10$\mu$m, and cannot be successfully anti-reflection overcoated. Its transmission is therefore about 70%. (A single element objective lens was used to minimize reflection losses, since calculations indicated that it would not limit the resolution over most of the field-of-view. In fact,

there is some justification for smearing the image over one resolution cell in any case, so that point sources cannot be "lost" behind the supporting grid structure.)

(It should be noted that the germanium objective lens provided with the HADIM can also be used on the HADIS. However, there is no great gain to be realized, since its extra diameter would be of no use, and its transmission is about 90%. It has a focal length of 38.1mm, which would change the field-of-view slightly.)

### 2.1.4 De-Dispersion

The method of de-dispersion is fairly clear from Figure 2 and the previous discussion. It is apparent from the grating equation (eq. 2), that if the roles of $\alpha$ and $\beta$ are reversed, the grating will cause wavelengths following the reverse paths to be diffracted at the common angle $\alpha$, thus being de-dispersed. Mirrors placed near the focal plane of the spectrograph cause this reversal of direction.

Both retro-reflecting mirrors have adjustable mounts. The upper mirror is critical to the spectral focusing of the instrument, and is so adjusted. Since quality of focus is no longer of importance after the final encoding of the data, the lower mirror is adjusted to redirect the light for optimum collection.

### 2.1.5 Detector Optics

In order to collect all the encoded energy, the detector must fill the exit pupil of the optical system. It is the function of the detector optics, or field lens, to make the exit pupil as small as possible. (Actually, de-dispersion is part of this process. Otherwise, a large detector could have been located directly behind the spectral mask.) Also, to eliminate variations of response for different parts of the field-of-view due to detector non-uniformities, it is advan-

tagious to focus the aperture stop itself onto the detector. These functions are accomplished by locating the field lens at the focus of the de-dispersed image (where its size can be minimum), using the fastest possible field lens, and locating the active detector at the image of the grating produced by the collimating mirror/field lens combination.

The lens was calculated to require a clear aperture of 8.25mm, and was designed for a focal length of 10mm. Its object distance is large (several meters), so it was optimized for 11.5$\mu$m wavelength with the conjugate at infinity. It is an f/1.18 optic, fabricated from KRS-5, and mounted to provide the required $6^{o}$ field-of-view.

In order to fill the exit pupil, the detector itself is required to be $\simeq$ 1mm on a side, oriented in the same way as the diffraction grating. It should be noted that immersion of the detector in a material of index-of-refraction $n > 1.0$ (e.g., germanium, for which $n \simeq 4.0$) would allow a proportionate reduction in the dimensions of the active element of the detector, with possible S/N improvement. This was done in the case of the HADIM, but not for the HADIS.

## 2.2 Timing and Bandwidth Considerations

The spatial/spectral encoding process for the HADIS involves cycling the spatial mask through its 1023 positions for each one of the 63 configurations of the spectral mask. Between each scan of the spatial mask, certain other data and functions must also be performed: First, there is need for a "dark sample" both before and after the spatial scan. The first dark sample must be taken before the coded portion of the mask has moved into place; the second one must wait until the mask has moved away from the field stop. Both dark samples should be taken with the same configuration of the

spectral mask in place. Second, the spectral mask must be indexed to a new configuration between spatial scans (but not so as to interfere with the above dark samples). Finally, as previously mentioned, there are 33 extra positions on the spatial code which must be considered as part of the scan, and thereby must be moved out of the way between the two aforementioned dark samples.

The speed at which the above sequence of events takes place has not yet been discussed. However, it is clear that high temporal resolution is a desirable feature, particularly in regard to potential applications of the technique for flight experiments; spatial/spectral frame times in excess of a few seconds are impractical. Then too, many detectors achieve better noise performance at higher frequencies, up to several hundred kHz. (This is true of biased photoconductors, for example, that exhibit a noise spectrum inversely proportional to frequency.) In general, should longer observation times be required to improve the S/N of a reconstructed scene, it can be better performed by co-adding several fast frames, rather than by slowing the whole encoding process.

There is a limit to the speed at which the HADIS can be operated, and it is determined by the 15msec required to change the position of the spectral mask. With this as a limit, we shall now investigate the operation of the instrument and the clocking of the data in the time domain.

### 2.2.1 Spatial Mask Timing

As previously determined, the spatial encoding disc has $66^{\circ}40'$ between the two encoded sections, during which time the dark samples are taken and the spectral mask stepped. If we assume that about $60^{\circ}$ of arc is then available to step the spectral mask, and assume there are about 15msec in which to do it, the allowable rotation speed is $\simeq$ 667 RPM.

In fact, a 720 RPM (12 revolutions/sec) motor was selected to drive the encoding disc, allowing about 14msec to increment the exit mask.

The spatial/spectral scan can now be described in terms of the times required for each part of the cycle.

(1) The 1023 mask code configurations change at a 41.472 kHz rate (i.e., a new configuration appears every 24μsec).

(2) The 1023 element sequence takes 24.67msec.

(3) The entire coded sequence (including the 33 extra configurations) takes 25.46msec.

(4) Dark samples are taken 0.8msec before and 0.8 msec after the coded sequence.

(5) An entire spatial frame (dark samples included) takes 27msec.

(6) The spatial scan periodicity is one every 41.7msec (i.e., 24 frames per second).

(7) An entire spatial/spectral sequence takes 2.6 sec.

The spatial mask drive was made to have continuous rotation, both for mechanical simplicity and so as to achieve a high sample rate. According to Gottlieb[4], a continuously moving mask acts exactly like a discretely stepped mask in every respect if the electronic sampling period is taken to be synchronous with the mask motion and proper phase is maintained. This has been accomplished in the HADIS by accurately positioned timing slits adjacent to the coded section, one timing slit for each of the 1056 coded mask configurations. These can be seen in Figure 4. Also seen are separate timing channels for "beginning of frame" and "end of frame", which are used to trigger the two dark samples.

The field stop has a matching set of single slits. Timing pulses are obtained when lines-of-sight exist between sets of lamps and photodiodes, through matched pairs of slits in the rotating mask and the field stop. The pulses generated by the rotation of the disc serve as the primary system clock, controlling various functions of the electronics and the clocking of the data to the computer.

### 2.2.2 Spectral Mask Positioning

The spectral mask also has three photo-sensed position indicating channels. In this case, however, they serve no timing function, but simply serve as a check on the motion of a stepper motor which serves to reposition the mask.

A spatial/spectral scan is always started with the spectral mask at one end of its motion. Initiation of a spatial/spectral scan by the computer software causes the stepper motor drive to "zero" the motor. This is done by slewing the lead-screw carriage past the end of the code, then stepping it back until the first position slit is aligned. The scan can then proceed as previously described. The stepper motor is automatically zeroed at the end of each complete scan. The software could easily be modified to allow the spectral code to be incremented in either direction.

### 2.2.3 Bandwidth Requirements

The ideal way to observe the HADIS signal would be to count photons incident on the detector during a sample period. The photon counter would then be reset to zero, the mask configuration changed, and a new observation started. In actuality, one must integrate the charge induced in the detector during a sample period, at which time a voltage proportional to the charge is read out. The integrator can be reset to zero at that time, and a new integration started.

If the period of integration is characterized by the time T, then the highest frequency that can be measured is on the order of 1/2T, corresponding to alternately high and low measurements. Noise at frequencies higher than 1/2T are then effectively filtered out by the integration process. To retain a high dynamic range, without sacrificing resolution, however, the response time of the detector must be much shorter than T. For example, if 12 bits (a factor of 4096) of dynamic range above the noise level is to be maintained, the detector response time $\tau$ is given by:

$$e^{-T/\tau} = 2^{1/12} \tag{7}$$

$$\tau \simeq T/8 \tag{8}$$

The associated preamplifiers and electronics must have a frequency response on the order of:

$$f = \frac{1}{2\pi\tau} \tag{9}$$

If we substitute the value T = 24μsec in the above equations, corresponding to the usual HADIS operation with a 720 RPM spatial mask drive, we find $\tau \simeq 2.9\mu$sec and f ≃ 55 kHz. Higher bandwidths will not hurt, in fact, but may be useful in extending the dynamic range. The effective bandwidth to use as a noise cutoff in evaluating a detector is given by 1/2T ≃ 20 kHz.

At the low frequency end, the HADIS signal is effectively "chopped" by the taking of dark samples before and after each spatial frame. This happens at approximately a 40 Hz rate, and represents the low frequency limit of the information bandwidth; noise at lower frequencies is effectively filtered out.

## 2.3 Detectors

As with other optical sensors, the more the noise of the system can be reduced, the better will be its sensitivity. The selection of low noise detectors can usually contribute toward this goal. Thus, having established the size and spectral range of the detector, the detector with the highest detectivity D* over the required frequency range should be used. This calls for the use of high performance quantum detectors. Since the bandwidth requirements go down to the comparatively low frequency of 40 Hz, unbiased photovoltaic detectors would be preferred to photoconductors which suffer from 1/f noise. Photovoltaic detectors of sufficiently large area are not available for the 8-14$\mu$ m region, however, so we must contend with the poor low frequency characteristics of a photoconductor.

### 2.3.1 PbSe Detector

Although the HADIS was designed to be used for wavelengths in the 8-14$\mu$m atmospheric window, it can be used in other spectral regions by simply changing detectors. The ready availability of a thermoelectrically cooled PbSe detector for the 2-5$\mu$m band, together with the secondary interest of that region because it also corresponds to an atmospheric window, prompted us to use it for most of the tests and analysis of the HADIS. There is no difficulty in extrapolating the analysis to different wavelengths, and the fact that it is also a photoconductive detector should produce similar performance characteristics to a photoconductor in the 8-14$\mu$m band. (In fact, a (Hg, Cd) Te detector was obtained for use with the HADIM over the 8-14$\mu$m band, and may be readily adapted to the HADIS. This was not done for reasons which are discussed more fully in Section 3.2.)

The pertinent characteristics of the PbSe detector are given in Table 2. Note that the dimensions of the active area (2mm x 2mm) are twice what was actually required by the HADIS optical design. Theoretically, this should double the noise over what would otherwise be expected.

The detector was installed in a housing containing the KRS-5 field lens. The housing also had provision for an order sorting filter, to reject short wavelength information transmitted through the spectrograph in orders of diffraction higher than the first. This assembly is provided with an adjustable mount, so its position at the dedispersed focal plane of the spectrograph can be optimized. The preamplifier is located in close proximity to the detector on the same mount.

### 2.3.2 Pyroelectric Detector

It was also of interest during the course of the program to investigate the performance of the HADIS using a pyroelectric detector. Being a thermal detector, it has a very broad spectral response including both the 2-5$\mu$m and 8-14$\mu$m bands. The characteristics of the pyroelectric detector used with the HADIS are listed in Table 3.

Not only is the noise of even a good pyroelectric detector much higher than that of most quantum detectors, but it also has the opposite characteristics with regard to its noise spectrum: high frequency noise dominates. In order to take advantage of the better detectivity at low frequencies, and to achieve better sensitivity through longer frame times, the entire HADIS operation was slowed down. The 720 RPM mask drive motor was changed to a 20 RPM motor. The times listed in Section 2.2.1 must consequently be increased by a factor of 36, and the bandwidth shifted downward by the same factor.

## Table 2: PbSe Detector Data

| | |
|---|---|
| Spectral range: | 2-5 $\mu$m |
| Wavelength of maximum response: | 4.3-4.5 $\mu$m, typical |
| Element resistance (dark): | 0.85 megohms, measured |
| Time constant: | 10 $\mu$sec, typical |
| Cooler power: | 1.2 Volts, typical<br>2.0 amperes, typical |
| Required power dissipation: | 2 Watts, typical |
| Operating temperature: | 253$^{o}$K |
| Element size: | 2 mm x 2 mm |
| Responsivity | 34,500 V/W, measured |
| $D^{*}_{\lambda_p}$: | $5.19 \times 10^{9}$ cm $Hz^{1/2}W^{-1}$, measured |
| Test conditions: | 500$^{o}$K blackbody<br>$6.25 \times 10^{-6}$ W/cm$^{2}$ power density<br>10 Hz noise bandwidth<br>840 Hz chopping frequency<br>100V bias<br>1 megohm load resistor |

## Table 3: Pyroelectric Detector Data

| | |
|---|---|
| Spectral range: | 1-25$\mu$m or greater (KRS-5 window) |
| Element size: | 1mm x 1mm |
| Test conditions: | $1000^{\circ}$K blackbody |
| | $300^{\circ}$K background |
| | $300^{\circ}$K operating temperature |
| | 6.51 mm dia. blackbody aperture |
| | 25 cm blackbody - detector distance |
| | square wave chopping |
| | $4.31 \times 10^{-4}$ W/cm$^2$ RMS flux density |
| | 7 Hz noise bandwidth |
| | x 105 preamplifier gain |
| | $10^{12}$ ohm load resistor |

Electrical measurements:

| Chopping Freq. (Hz) | Signal (mV) | Noise (mV) | Responsivity (V/W) | $D^*$ (cm Hz$^{1/2}$W$^{-1}$) |
|---|---|---|---|---|
| 15 | 1300 | 0.120 | 2880 | $6.65 \times 10^8$ |
| 90 | 230 | 0.030 | 510 | $4.7 \times 10^8$ |

The pyroelectric detector was installed in a housing and mount similar to that described for PbSe detector. Its preamplifier was also located on the mount, and provision was made for order sorting filters. The sensitive element was hermetically sealed in a cavity, to prevent degradation due to the hygroscopic nature of the pyroelectric material, with the KRS-5 lens serving also as the window.

## 2.4 HADIS Electronics

Electronics for the HADIS is housed in five major physical (and functional) groupings: (1) the detector preamps, which are mounted in close proximity to their respective detectors; (2) preamps for the timing light circuits, contained in a separate chassis attached to the main electronics box; (3) the main electronics assembly, consisting of card mounted circuits and power supplies contained in a box bolted on one end of the spectrograph; (4) the driver for the exit mask stepper motor, which is remotely rack mounted in the computer/display facility console; and (5) a "computer simulator", to enable operation without the active use of a computer. The first three items listed may be seen in the HADIS photograph, Figure 2. In addition, there are interconnecting wiring harnesses and appropriately mounted lamps and photodiodes to generate the timing signals.

The functions of the electronics are to amplify the signal generated by the detector; to integrate the signal over periods corresponding to each of the discrete mask configurations; to digitize the integrated levels; and to transmit them, together with the corresponding clock or synchronization pulses, to the computer for analysis. A block diagram of the HADIS electronics is given in Figure 6

### 2.4.1 Detector Preamplifiers

Preamplifiers to match the characteristics of the aforementioned PbSe and pyroelectric detectors were designed and constructed to mount in the same assemblies that hold the detectors. The bandwidth requirements discussed in Section 2.2.3 were applied to the PbSe detector preamp; the pyroelectric detector operates with a frame time a factor of 36 slower, so the bandwidth requirements were correspondingly reduced. Power for both preamps is obtained

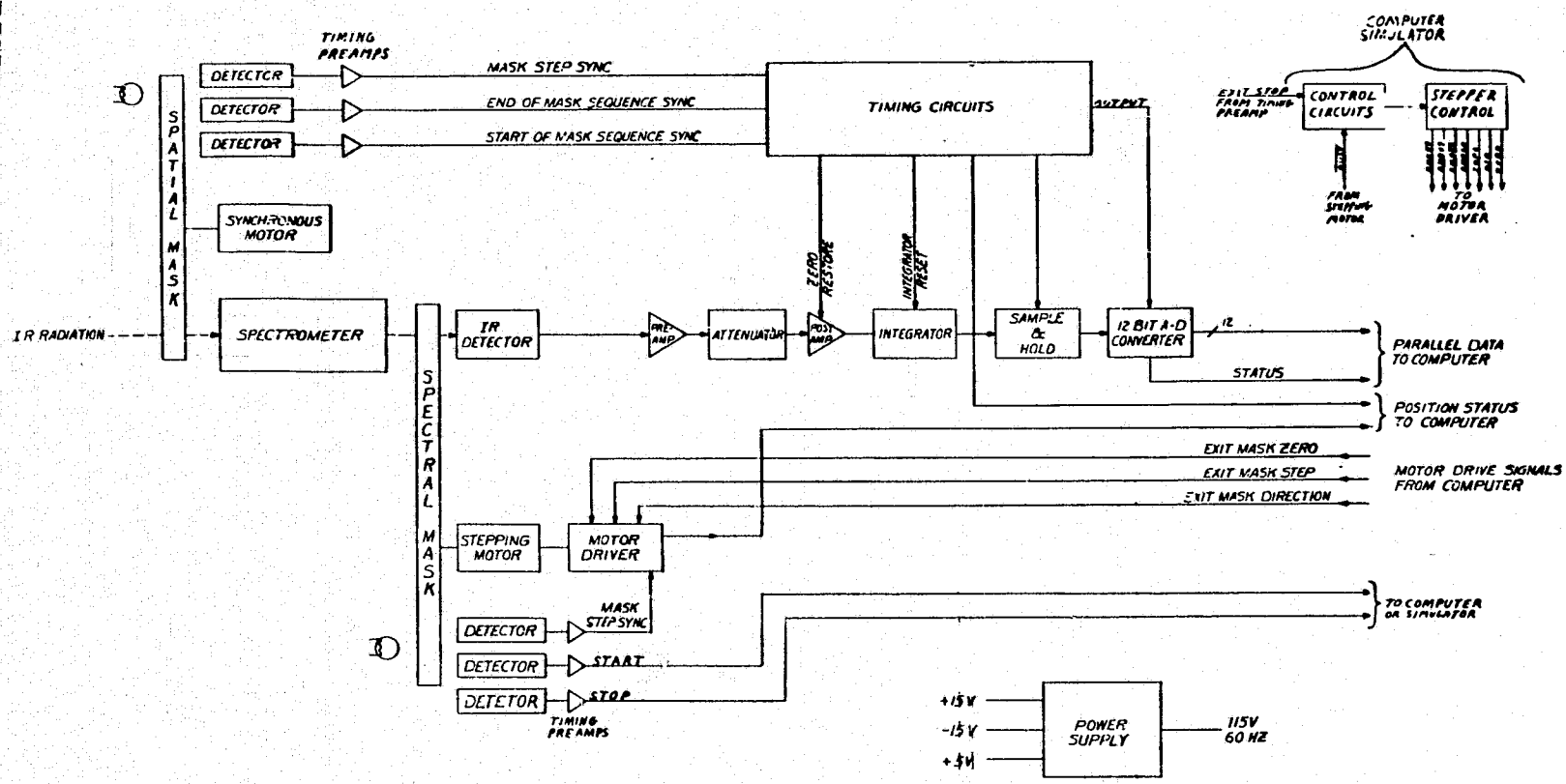


Figure 6. HADIS Electronic Block Diagram

from power supplies contained in the main electronics box. (In the case of the PbSe detector, power for its thermoelectric cooler and its bias voltage must be provided by external power supplies.)

### 2.4.2 Timing Electronics

Timing signals are generated electro-optically from the timing marks on the two encoding masks, which were described previously. Each mask has three separate timing channels: one to indicate the start of a mask sequence, a second to indicate each of the mask code configurations, and a third to indicate the end of a mask sequence. The timing channels all have their own incandescent bulb and photodetector, the signals from which are amplified and shaped into square pulses by the timing preamplifiers.

The shaped pulses from the spectral mask are interfaced, via cables, directly to the computer (or a "computer simulator" - see Section 2.5) and to the stepper motor drive control. In the case of the spatial mask, the timing pulses are sent to the timing card in the main electronics box. There, they are processed to generate DC restore pulses, reset pulses for the signal integrator, commands for the sample/hold and A/D converter modules, a monitor synch signal and a stop pulse to inform the computer of the end of a field.

### 2.4.3 Main Electronics Assembly

The main electronics box contains timing circuits, an amplifier/attenuator card with DC restoration circuits, an active integrator, a sample/hold module and an A/D converter module, together with their power supplies, wiring harness and connectors, and a buffer card to transmit the digital signals to the computer.

The detector preamp output is connected through a coaxial cable to the amplifier card in the main electronics box. Here, the signal passes via a high impedance buffer and a selectable attenuator (5 positions, at 10 db per step) into a post-amplifier stage. True integrals of the amplified signal are then obtained by an active integrator, over timing intervals corresponding to a single mask configuration. At the end of each such interval (about 25$\mu$sec), the value of the signal on the integrator capacitor is sampled and held, and the integrator is immediately discharged to zero in about 0.2$\mu$sec). Integration of the next 25$\mu$sec sample is then started, while the A/D converter converts the "held" signal into a 12-bit digital number. This conversion takes about 20$\mu$sec, at which time a status pulse causes the computer to accept the data; the sample/hold and A/D modules are then ready to accept the next integrated level.

A typical Hadamard signal consists of dark zones, representing no signal on the detector, and light zones comprising small variations about some average level somewhat separated from the dark zone levels. Since the structure of these smaller variations contains most of the interesting information, the first sample of the light zone signal is clamped to zero volts by a capacitive DC restore circuit. This assists in placing the information content of the fine structure (light zone) somewhere near the middle of the $\pm$ 5V range of the A/D converter. By these means, the fine structure may be examined at gain levels yielding the maximum signal range of the A/D converter, even though the dark zone signal is saturated.

It should be noted that the repetition of the first 33 mask code configurations at the end of each field is useful to remove, to first order, the effects of low frequency noise, since the corresponding (identical) signals can be matched over that time interval. The low frequency time constants of the signal processing are in excess of 5 seconds for the PbSe detector (and over 30 seconds for the (Hg, Cd) Te detector used with the HADIM), so the signals can be regarded as essentially DC coupled.

While on the subject of dark zones, it should also be noted that dark samples taken before and after stepping of the exit mask can be used to correct spatial/spectral data for varying emissivity of different portions of the spectral mask. This is, of course, subject to the effects of noise differences between the two dark samples.

### 2.4.4 Stepper Motor Driver

The controller, which drives the stepper motor to position the spectral encoding mask, is a commercial unit designed specifically to provide the required number of pulses to the motor. A series of 14 pulses are required to move the mask the 0.007" incremented spacing. Timing of this sequence is accomplished through computer (or "computer simulator - see Section 2.4.5) generated commands; therefore, the controller is located near, and interfaced with, the computer. The stepper motor control is interlocked with two limit switches and the exit mask timing marks, to avoid accidental overdrive and to properly initialize the start of the scan.

### 2.4.5 Computer Simulator

The computer simulator is a separately packaged unit, rack mountable. (See Figure 7). It generates the proper set of pulses to control the stepper motor in lieu of a computer. It operates in conjunction with the main electronics "stop" pulses to move the exit mask in any one of four modes: (1) stop, (2) sweep once and reset, (3) sweep once (i.e., in one direction only, so that a second frame would cause a sweep in the opposite direction), and (4) sweep continuously, for spatial/spectral frame integration. The usefulness of the computer simulator would be primarily for flight experiments, where data would be recorded on magnetic tape for later analysis.

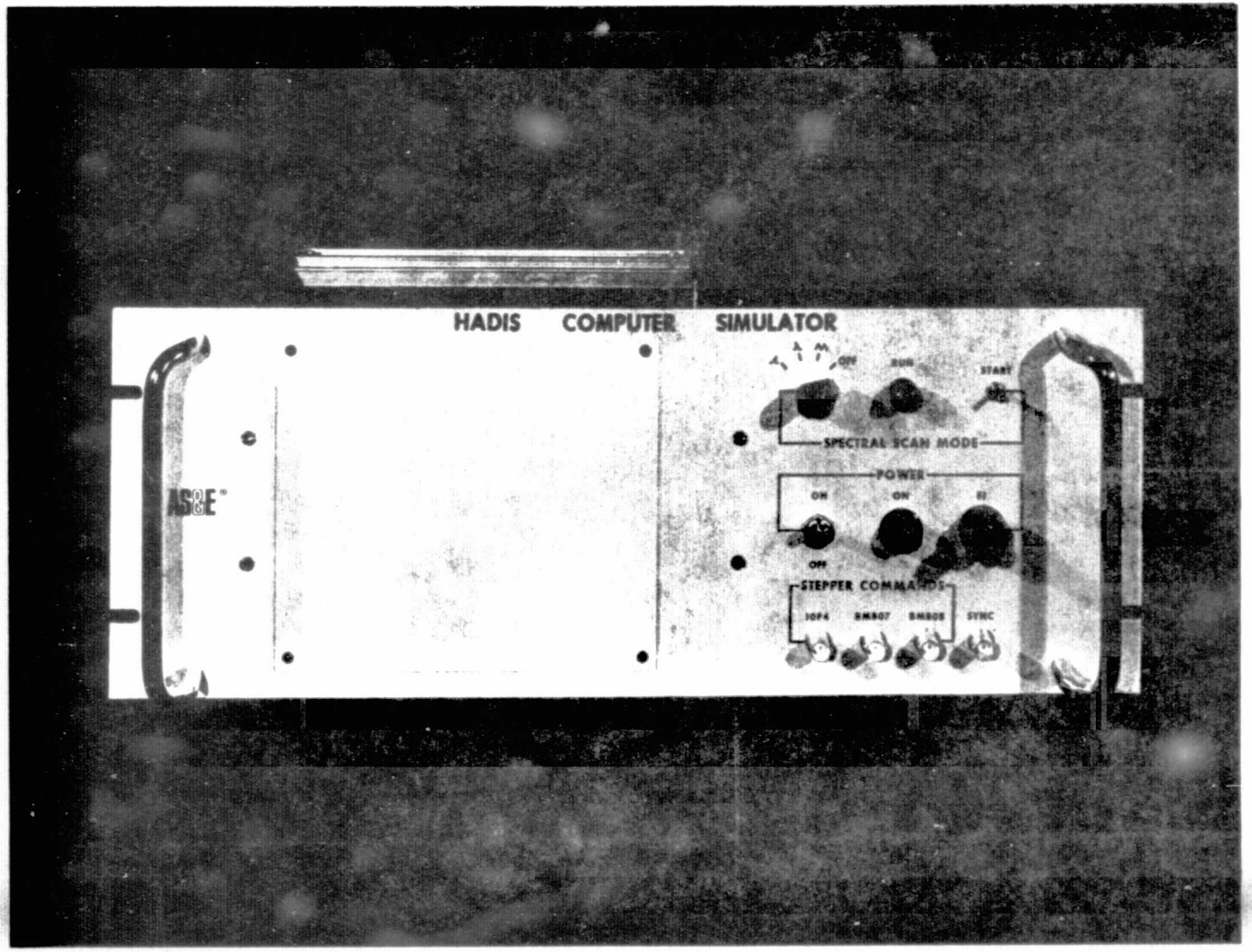


CY-113

Figure 7. HADIS Computer Simulator

## 3.0 HADAMARD TRANSFORM IMAGER

The Hadamard transform imager (HADIM) is essentially a subassembly of the HADIS. It uses the same spatial encoding assembly and most of the same electronics, eliminating only those functions that dealt specifically with the exit mask driving and synchronization. The software is simpler, in general, since decoding of spectral information, synchronization of entrance and exit mask drives, and reassembly of spatial/spectral information are not required. (The software required for obtaining purely spatial images with the HADIM can, in fact, be used to obtain spatial only images with the HADIS. This was done for much of the HADIS testing and evaluation, in order to save processing time.)

The HADIM was built primarily to achieve greater sensitivity than the HADIS with a much faster frame time. It is no longer limited by the optical speed of the spectrograph, so it can collect a much higher light signal (although a larger detector is required). It is provided with a cryogenically cooled, photoconductive (Hg, Cd) Te detector optimized for the 8-14$\mu$m spectral region. Its spatial field-of-view is nearly identical to that of the HADIS. Photographs of the HADIM are shown in Figure 8. Only areas of difference from the HADIS will be described in detail.

### 3.1 Opto-Mechanical Layout

The optical path of the HADIM, and the relative locations of its main components, are shown in Figure 9. The scene is focused onto a portion of the encoding mask determined by a fixed field stop. Light passing through the mask and field stop is collected by the field lens (which also serves as the vacuum window in the detector dewar), and focused onto the detector. The detector itself is immersed in a germanium hemisphere to reduce the area of the sensitive element.

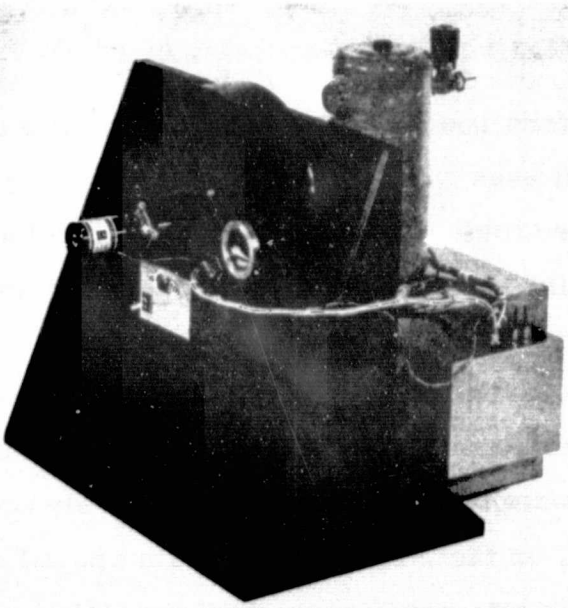

CY-115

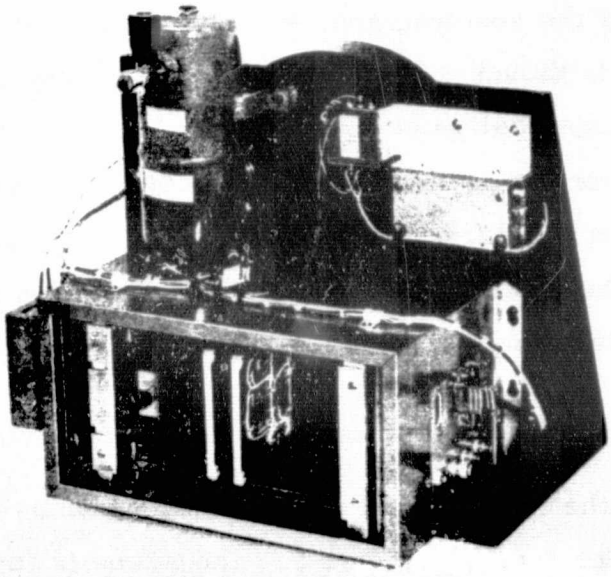

CY-127

Figure 8. Photographic Views of the Hadamard Imager (HADIM)

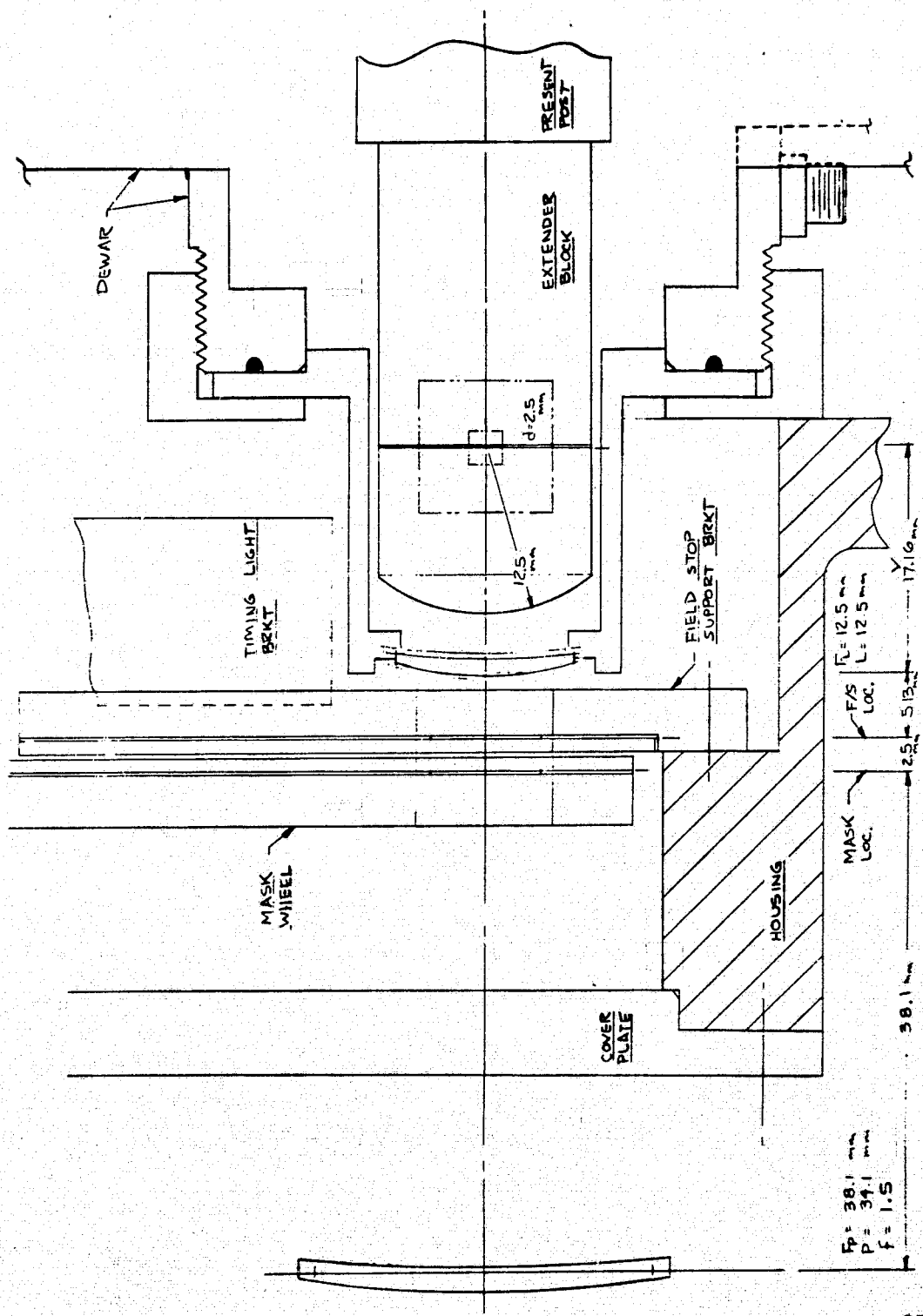


Figure 9. Optical Layout of the HADIM

ORIGINAL PAGE IS
OF POOR QUALITY

We note that in the HADIM optical design the objective lens is focused onto the detector by the field lens, and vice versa. Since the lens is conveniently made round, and the detector square, we arrange the optics so that the image of the detector is inscribed in the lens. Otherwise, the detector would have excessive area that would contribute to its noise output, but would contribute nothing to the signal. The detector itself is then the aperture stop of the system, as well as the exit pupil, and its image in the objective lens is the entrance pupil. As in the HADIS design, we can optimize the S/N by maximizing the entrance pupil, while using the fastest possible field lens to keep the exit pupil to a minimum.

### 3.1.1 Objective Optics

The HADIM was designed to have a nominal resolution of 5 milliradians. Since the encoding mask dimensions were pre-determined by the HADIS design, this requirement calls for a similar focal length $\simeq$ 34mm. A suitable Ge lens, designed and overcoated for 10.6$\mu$m, with a focal length of 38.1mm, and which could be mounted with a clear aperture of 34.1mm (f/1.12) was commercially available. Its focal length is close enough to the design goal to be acceptable. A resolution cell at this focal length subtends 4.5 milliradians, and the total field of view (wedge-shape distorted as before) subtends $8.03^{\circ} \times 8.55^{\circ}$.

### 3.1.2 Field Lens

The point that the field lens should be as fast as possible has already been made; it is impractical to consider having this lens substantially faster than f/1. Furthermore, it must have a diameter large enough to slightly overfill the spatial field stop (in the diagonal direction), so as not to vignette the corners of the field. Although the diagonal dimension of the field stop is only 8.25mm,

the field lens must actually be located some distance away from the plane of the field stop. There is considerable divergence of the rays due to the speed of the objective lens. Ray tracing showed the required clear diameter to be 12.5mm, which is then taken as the focal length as well.

The lens must have an object distance of 45.7mm, its distance from the objective lens. Its image distance, or the distance to the detector focal plane, is then calculated to be 17.16mm. Such a lens, with shape factor optimized for the above geometry, and anti-reflection coated for 10.6μm, was obtained. It was supplied to the detector manufacturer for installation in the dewar, where it serves as the vacuum window as well.

### 3.1.3 Exit Pupil

The dimension in the detector focal plane that corresponds to the diameter of the clear aperture of the objective lens is:

$$34.1\text{mm} \times \frac{17.16}{45.7} = 12.8\text{mm} \qquad (10)$$

A square detector having a 12.8mm diagonal is 9.05mm on a side. If the detector is immersed in a hemisphere of material having an index of refraction n, the focal plane is not changed, but the required size of the detector is reduced by n. Germanium has an index of refraction of 4.0 at 10μm, and was used as an immersion material. The required detector must then be 2.26mm on a side. Actually, in order to allow a safety factor for slight misalignments and aberrations, the detector specification called for 2.5mm x 2.5mm. This is then the exit pupil of the HADIM optical system.

### 3.1.4 Entrance Pupil

Working the above calculation in reverse yields the size of the detector image at the objective lens:

$$(2.5\text{mm} \times 4) \times \frac{45.7}{17.16} = 26.63\text{mm} \qquad (11)$$

The diagonal dimension of this square image is then 37.7mm, which is only slightly larger than the clear aperture of the objective lens. What this means, in effect, is that there is a slight amount of detector area, in the corners, which contribute unnecessary noise. The area of the entrance pupil is given by the area of overlap of the lens and detector image; it is calculated to be $6.97\text{cm}^2$.

## 3.2 (Hg, Cd) Te Detector

The detector obtained for use with the HADIM is a liquid nitrogen cooled (Hg, Cd) Te photoconductor, having a cutoff wavelength at 14μm. Large area (Hg, Cd) Te detectors for use in the 8-14μm band had not previously been immersed, so a special detector development was required. The main obstacle was to develop a suitable procedure to bond the detector chip to the germanium. Not only did the bonding agent have to be transparent over the wavelength range, and create a reasonable match in refractive index, but the handling procedure could not be guaranteed not to degrade the noise performance of the detector. While a maximum theoretical improvement of a factor of 4 in effective D* could be achieved, equal to the optical reduction in size, it was expected that a factor of 2 to 3 would be more realistic. Consequently, the detector was specified for a minimum D* value before immersion of $5 \times 10^9$ cm $\text{Hz}^{1/2}$ $\text{w}^{-1}$, at a chopping frequency of 40 kHz. Furthermore, specifications were placed on the bonding agent that

allowed no absorption dips larger than a factor of two over the 8-14$\mu$m band.

The detector's measured performance, before and after immersion, is summarized in Table 4. The basic data in the table was provided by the detector manufacturers; certain quantities in the table were computed from the manufacturer's data.

Physically, the immersed detector was mounted on the liquid nitrogen cooled cold-finger of a side-looking dewar. The dewar hold-time is four hours. The field lens of the HADIM serves as the vacuum window of the dewar, and the orientation of the detector is such that its sides are parallel to the edges of the field of view of the HADIM.

## Table 4: (Hg, Cd) Te Detector Data

| | |
|---|---|
| Wavelength range: | 8-14 μm |
| Element size: | 2.5 mm x 2.5 mm |
| Immersion: | 12.5 mm radius Ge hemisphere |
| Test conditions: | 77°K operating temperature |
| | Flat Irtran-2 dewar window |
| | 1000°K blackbody |
| | 0.127 cm dia blackbody aperture |
| | 0.41 chopper factor (square wave) |
| | 10 Hz noise bandwidth |
| | 10 kHz chopper frequency |

Un-immersed Measurements:

37 cm blackbody - detector distance

$6.69 \times 10^{-6}$ W/cm$^2$ power density[1]

68 ohm detector resistance

x6800 amplifier gain

| Bias (mA) | Signal (mV) | Noise (mV) | $R_{BB}$[1] (V/W) | $R_{\lambda p}$ (V/W) | $D^*_{BB}$[1] (cm Hz$^{1/2}$W$^{-1}$) | $D^*_{\lambda p}$ (cm Hz$^{1/2}$W$^{-1}$) |
|---|---|---|---|---|---|---|
| 16 | 92 | .051 | | | | |
| 20 | 109 | .059 | 38.3 | 110 | $3.5 \times 10^9$ | $1.1 \times 10^{10}$ |
| 24 | 128 | .070 | | | | |

Immersed Measurements:

47.5 cm blackbody - detector distance

$4.07 \times 10^{-6}$ W/cm$^2$ power density[1]

39 ohm detector resistance

x12000 amplifier gain

Table 4 (Cont'd)

| Bias (mA) | Signal (mV) | Noise (mV) | $R_{BB}$ (1) (V/W) | $R_{\lambda p}$ (V/W) | $D^*_{BB}$ (1) (cm $Hz^{1/2} W^{-1}$) | $D^*_{\lambda p}$ (cm $Hz^{1/2} W^{-1}$) |
|---|---|---|---|---|---|---|
| 40 | 450 | .076 | | | | |
| 48 | 540 | .090 | | | | |
| 56 | 624 | .100 | 12.8 | 46 | $4.8 \times 10^9$ | $1.7 \times 10^{10}$ |
| 64 | 707 | .120 | | | | |

(1) Note: Computed or estimated from manufacturers data.

## 3.3 HADIM Electronics

The electronics for the HADIM is the same as that used for the HADIS except for two features which do not require elaborate description: (1) The preamplifier, commercially obtained, was designed to match the characteristics of the (Hg, Cd) Te detector over the operating bandwidth of the instrument; (2) the preamplifier requires a highly regulated voltage, which is obtained from the power supplies in the main electronics box by extra regulation. This is done in a junction box located near the detector, and may be seen in Figure 8.

Of course, many functions of the HADIS electronics are not required by the HADIM. These include, specifically, the exit mask drive, its controller, and the corresponding timing circuits. The computer simulator has no function for the HADIM.

## 4.0 DATA PROCESSING

This section describes the actual equipment used for processing and display, the FORTRAN routines needed by HADIM and HADIS, and a brief discussion of the assembly language routines. Each routine is discussed separately as to its function and briefly as to its construction. In certain instances, where the software was dictated somewhat by the operating requirements of specific hardware, it has been necessary to identify the hardware and its manufacturer rather than using generic descriptions. The discussion assumes that the reader knows the elements of FORTRAN IV or V.

### 4.1 Processing and Display Facility

The Hadamard processing and display facility, shown in Figure 10, consists of: a Data General Corporation's NOVA 1200 Jumbo minicomputer with 32K of 16 bit core, hardware multiplier/divide, clock and hardware floating point options; a 1.25 mega-word disc cartridge memory for file storage; an 800 bpi, 45 ips tape recorder; an alphanumeric CRT terminal with edit option; a standard teletype; and a data display system which utilizes a Ramtek, Inc. computer/TV scan converter capable of 8 modes of graphic and image 4 bit data display plus a color TV monitor.

### 4.2 FORTRAN Software

The software consists of: Data General Corporation's RDOS disc operating system; FORTRAN V, which features global optimization, bit manipulation and very flexible I/O; assembly language I/O drivers to the special peripherals used in the system (HADIM, HADIS, RAMTEK); and FORTRAN routines as will be described herein.

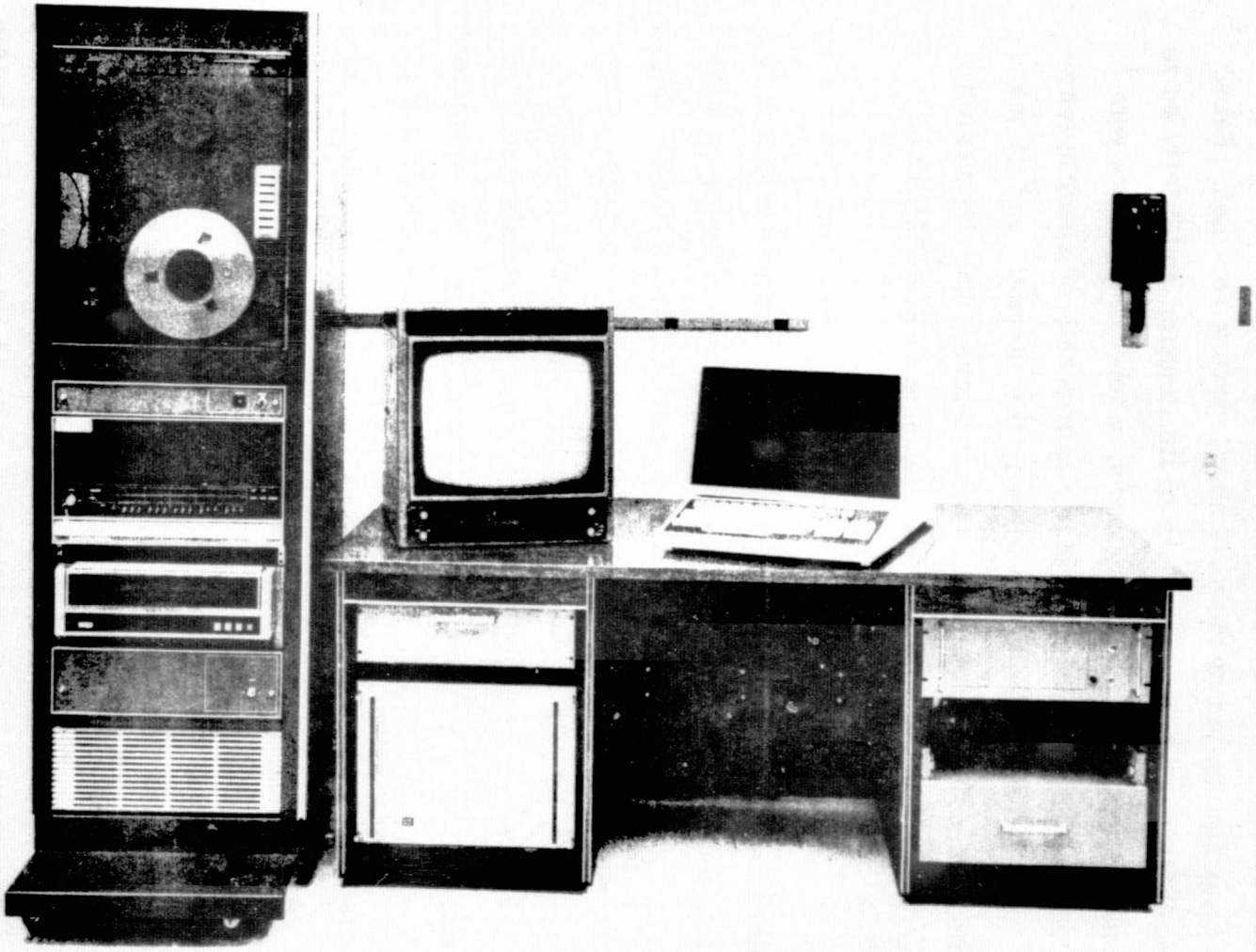

CY-077

Figure 10. Hadamard Processing and Display Facility

### 4.2.1 HCODERD

This routine acquires HADIM spatial Hadamard encoded "background" frames of 1058 or 1056 points each and integrates the frames as desired by the operator, keeping the 1058 or 1056 point frames separate. (This separation is required because the reflectivity and/or emissivity of the two Hadamard masks on the wheel are different. They were distinguished by deleting the last two timing slits on one of the masks, so it produces two less clock pulses that the other mask.) The two separate and integrated mask data are then stored separately as floating point data sets, on disc. The purpose of the routine is to store the emissivity variations and other systematic effects to remove them from the actual image data. The frames are normally taken with the field of view obscured. A representative flow diagram appears in Figure 11.

### 4.2.2 HCODERT

This routine acquires HADIM spatial Hadamard encoded frames of 1058 or 1056 points each, sums and thus integrates them, subtracts the appropriate background frames obtained from the disc, recorded there by HCODERD, and then combines the subtracted 1058 and 1056 data to form the raw, untransformed data. A 1023 element subset of these data are then Hadamard decoded by first a preordering array, IP1, then by an FHT algorithm and finally by a post-ordering array, IP2. After decoding, the one-dimensional array is factored into a two-dimensional 31 x 33 form for display purposes. After display the routine calculates the RMS value of all image points; this is useful for data taken with a blocked system to determine S/N ratios. A representative flow diagram appears in Figure 12.

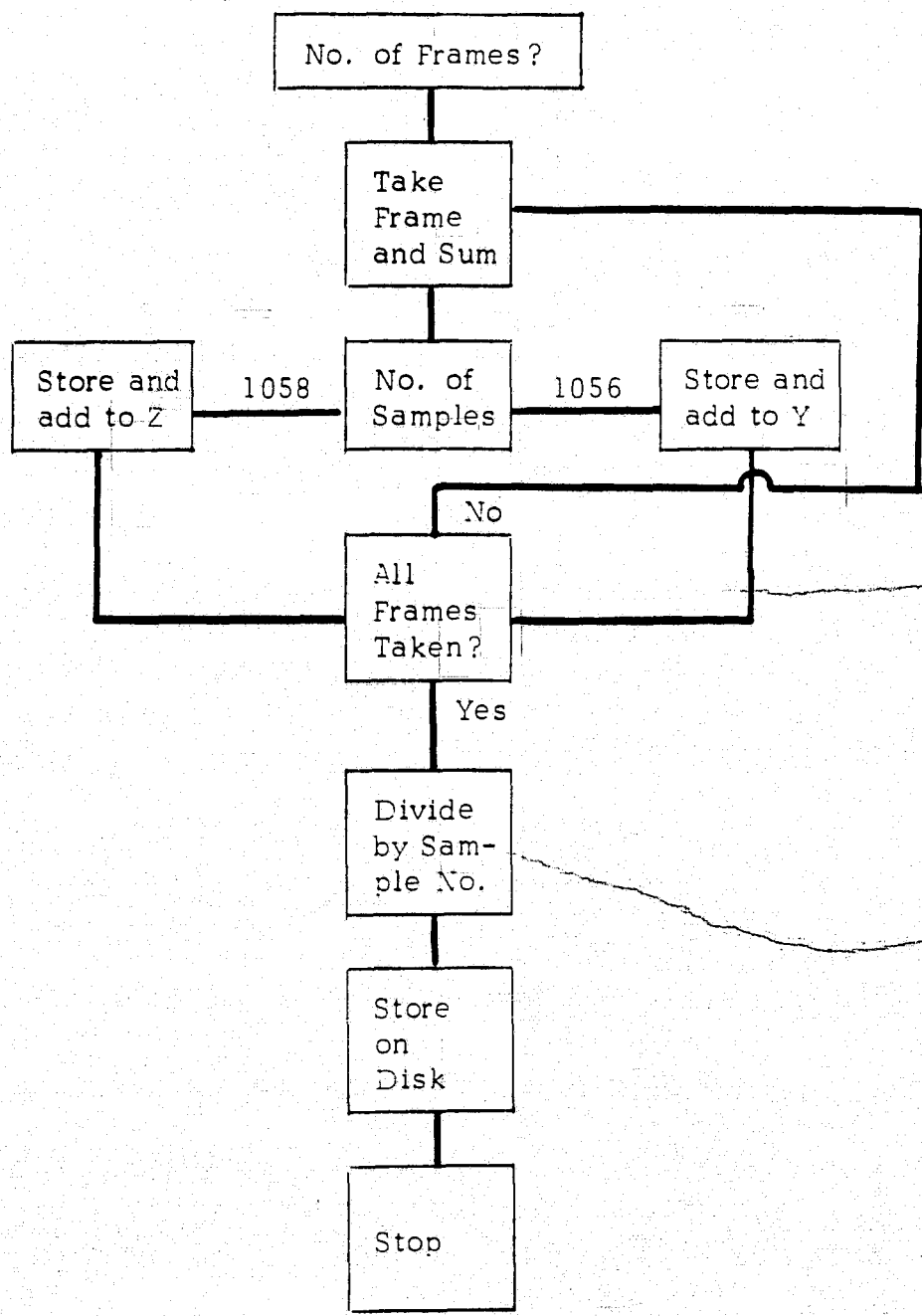




Figure 11. Flow Diagram for the HCODERD Routine

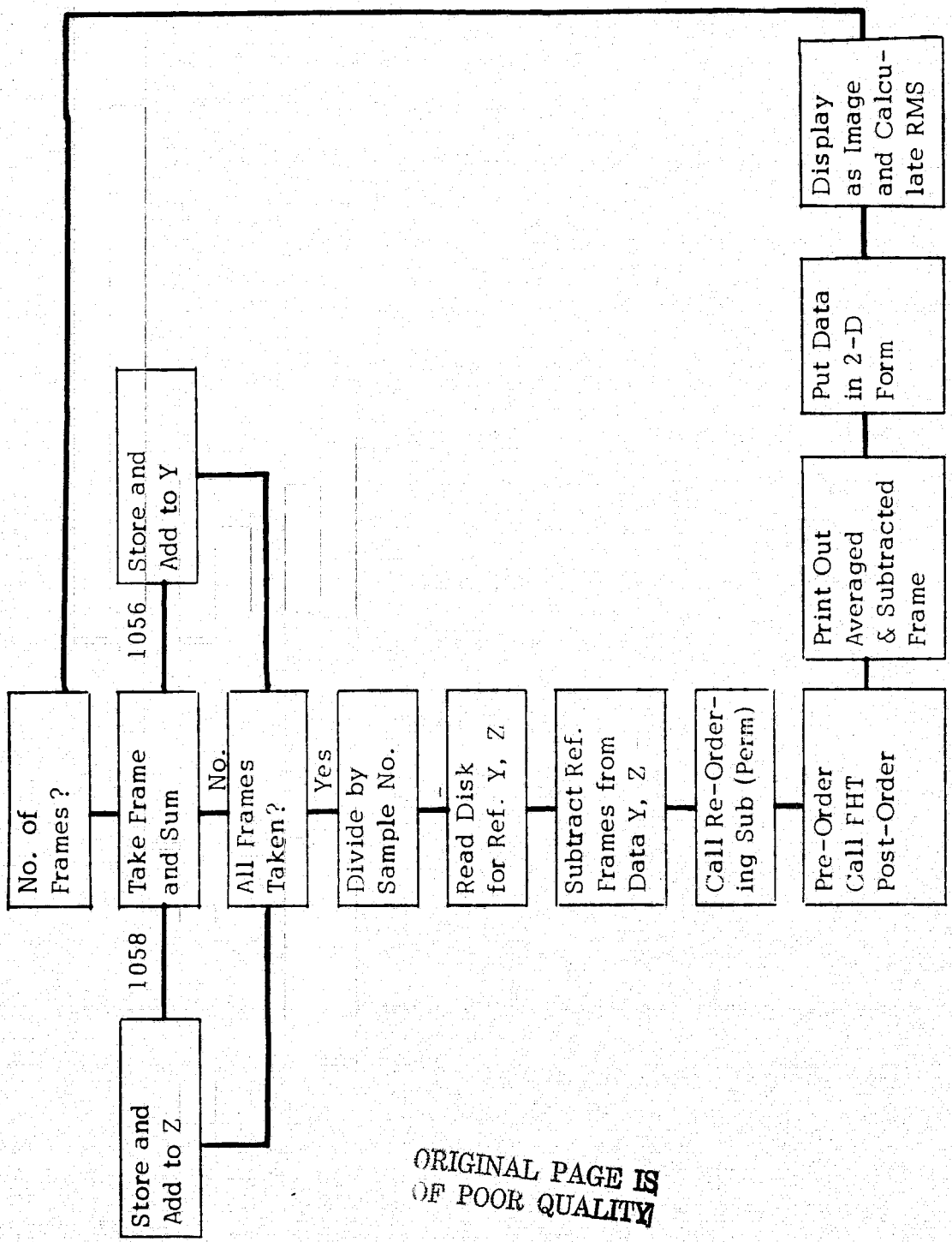






Figure 12. Flow Diagram for the HCODERT Routine

### 4.2.3 FHT

This routine performs the Fast Hadamard Transform in a manner exactly analogous to that performed by standard Fast Fourier transform routines except that only real variables and real addition and subtraction are needed. The present algorithm was developed from Nelson et al.[7] The "DO" loop at the beginning of the routine is used only for encoding; it provides the proper beginning for the first element.

### 4.2.4 PERM

This routine calculates the IP1 and IP2 re-ordering arrays which allow decoding via the S-matrix ( of Nelson et al[7]), and are necessary in conjunction with the Fast Hadamard Transform basic algorithm, just as binary bit inversion (also a re-ordering sequence) is necessary to use in conjunction with the Fast Fourier transform algorithm.

The re-ordering arrays are generated in PERM by first producing the appropriate Hadamard array. The $2^N$ elements of the Hadamard array are completely determined by the first N elements, which are arbitrary. The first N elements do produce the phase of the resulting transformation, however. Hence the 3rd argument of this routine's calling sequence is used to determine the first N elements of the Hadamard array and also (via the sign) the direction of the array.

The exact procedure for producing the pre- and post- re-ordering arrays and the $2^N$ Hadamard elements given the first N, is clearly described in Reference 7.

### 4.2.5 PIXD

This routine displays the 31 x 33 pix array, one horizontal line at a time. First the entire array is searched for the maximum value, then, as each line is generated, each element is normalized so that the maximum element is integer 15. Any element less than 0 is set to 0. A line is displayed twice to create a larger displayed image. Each line consists of 31 integer numbers which have a linear image of 0-15 in value.

### 4.2.6 PIXOA

This routine first re-orders the intensity values of 0-15 to fit the Ramtek unit's bit arrangement, provides initial mode instructions and finally provides data to the Ramtek I/O driver in the form of two elements per word. The elements are doubled to double the displayed image size. Octal and bit manipulation are used to provide the display language instructions in FORTRAN. The Ramtek driver requires the first location of the instruction table and the number of instructions to be transmitted.

### 4.2.7 HDCODEF

This routine performs the two-dimensional, spatial-spectral Hadamard decoding of HADIS data. The exit mask is first zeroed. The data are acquired by HDCODEF as spatial data, a number of frames at a time to integrate, and then the exit mask is stepped to provide another Hadamard wavelength configuration. This process is repeated until all 63 exit mask positions are included. Thus, 63 x 1058 integrated data points are taken of which 63 x 1023 are used. These data points are stored on disc, two integrated spatial frames (two Hadamard spectral samples) at a time. The disc storage is designed to minimize disc I/O, particularly disc head movement.

The 2048 word core buffer is one dimensional to provide for storage of either 63 point sets or 1023 point sets. Equivalence could have been used with two, two-dimensional buffers if desired. The detailed rationales for disc storage configuration is covered in more detail under HTRND. After complete transfer of all data to disc, HDCODEF zeros the exit mask, calls the decoding routine HTRND and, after transformation, closes the disc file.

### 4.2.8 HTRND

The two-dimensional Hadamard decoding is performed by HTRND. This routine calls PERM and FHT and uses the same decoding method as used in HCODERD. However, as a two-dimensional transform is required, two, one-dimensional transforms, are performed with the Hadamard transform of the 1023, 63 point columns decoded first from the raw data. The once transformed data are then Hadamard transformed as 63, 1023 point rows. This second transform produces a correct two-dimensional Hadamard decoding of the optically encoded data (see Gottlieb).

The complexity of this routine results from the relatively small core of our dedicated computer system. Rather complex disc I/O is required to store efficiently the data in various stages of transformation with minimal disc head motion. The method used to accomplish this is to sub-divide the 63 x 1023 array into sub-arrays of 2 x 32 elements each, with each sub-array to be addressed as a logical record from the disc. A set of such sub-arrays can then be addressed to form a 2048 word band of rows or columns (32, 63 point columns or 2, 1023 point rows) which can then be Hadamard transformed and re-stored on disc. Thus a minimum number of records need be located by the disc heads. Even with this complex method of data storage, the column transformation takes almost an order of magnitude longer than the row transformation.

### 4.2.9 HPIXF

This display routine is used to produce a set of 12 contiguous spectral images, starting at a given number properly re-assembled and with their respective wavelengths shown on the CRT terminal. It utilizes a sub-routine, HPIXSF which displays a given image, writes the calculated wavelength and locates the image at an appropriate part of the TV screen. HPIXF determines the proper screen positions, the maximum value of all data (determined before any picture is displayed) and the wavelengths corresponding to the spectral images displayed. This latter part requires knowledge of the wavelength dial setting used by HADIS.

### 4.2.10 HPIXSF

This routine produces a correctly re-assembled spectral image which represents a truly monochromatic slice, and displays same on the color TV screen via PIXD plus the wavelength and maximum pixel value on the CRT terminal. The re-assembly is accomplished in a very straightforward but time-consuming manner by reading in, from disc, a set of two 1023 point rows, then utilizing only one display column of 33 points from one of the read-in image rows. The 31 x 33 re-assembled spectral image is built up by repeating this process 31 times. The image array is then displayed and corresponding wavelength written out.

### 4.2.11 HSPEXF

This routine displays a "summed" image of the scene, a pseudo-color gray scale and then allows the experimenter to visually select a particular pixel of the scene and have the pixel's spectrum displayed. To do this, the entire set of data is read in from disc 2048 words at a time and used to find the maximum value and pro-

duce an array whose pixels represent the summed or integrated value under the spectral curve for that pixel. The array is displayed by PIXD and a pixel cursor location requested, as the designation of two signal integers representing the cursor's two coordinates (0, 0 represents the "home" position of element 512 out of 1023 elements or the center of the scene). Via sub-routine CURSOR, the image is re-displayed with the pixel at the cursor location changed to black or white depending on the covered pixel's intensity. HSPEXF then plots the spectrum of the chosen pixel on the TV screen, adjacent to the image, by reading from disc. This plot has a zero line and end-point wavelength values. The plot of intensities vs wavelength is also written out on the CRT terminal. Wavelengths are determined as in HPIXF.

### 4.2.12 CURSOR

This routine accepts the operator's wishes for the relative positional change in a black or white image cursor pixel; re-displays the image via PIXD with the new cursor location in black or white, depending on whether the intensity of the replaced pixel is higher or lower than one half of maximum, respectively; and computes the pixel number in order for the calling program to display the pixel's spectrum. The value of the replaced pixel is stored so that the pixel can be re-displayed when a new cursor position is desired.

### 4.2.13 PLOT

This Ramtek routine provides the necessary instructions to plot the spectrum of a particular pixel. The spectrum is plotted, starting with given coordinates and spectrum length. A base line is first plotted, then the data points are plotted with a vector drawn between adjacent data points. The same Ramtek I/O driver is used as in PIXOA.

### 4.2.14 RAMN

This Ramtek routine takes a floating point number and displays it, with decimal point, at any given starting coordinate. Two calls to this routine, with different starting points and numbers appropriate to the shortest and longest wavelengths of the plotted spectrum of a particular pixel, give an indication of the spectrum's wavelength range. This routine uses the same Ramtek I/O driver as PIXOA.

## 4.3 Assembly Language Routines

There are three assembly language routines all of which are I/O drivers. The first one, called HADIS, accepts the timed Hadamard samples from either the HADIM or HADIS instruments. The samples, produced by a 12 bit A/D converter, are clocked in through the NOVA 1200 data channel (Direct Memory access) so that no accumulators are used during the sample transfer process. HADIS sets up the data channel flags, sample count and input registers; waits for the first timing pulse from the wheel after being called from the FORTRAN V program; and then returns to the calling program after the end timing pulse occurs, indicating that all data has been transferred to core. The sample count is also stored in memory by this routine.

STEP is an I/O routine that can either step the HADIS exit mask by one position either way depending on the argument sign or will zero the exit mask to its reference position by a zero argument. The TTL pulses produced by the NOVA hardware associated with STEP are amplified and used to drive the stepping motor in the HADIS exit mask assembly.

RMTK is the final I/O driver routine. It communicates with the Ramtek display system, passing appropriate 16 bit instructions to the

display unit direct from the NOVA memory. The routine handles the data channel setup as was briefly described under the HADIS routine. In this case an output register is used. The FORTRAN V calling program must give RMTK the instruction data table location and, as a second argument, the number of instructions. The routine assumes no responsibility for the formation of the actual Ramtek instructions.

## 5.0 HADAMARD IMAGING SPECTROMETER (HADIS) TEST PROGRAM AND RESULTS

The purpose of the HADIS test program was to verify the HADIS technique by conducting the following tests:

a) Point Source Imaging

b) Extended Source Imaging

c) Wavelength Calibration

d) Spectral Imaging

The quantitative results of the above tests are discussed in detail in Section 7.0. In summary, the Hadamard advantage was successfully demonstrated, however, the sensitivity for this particular instrument required the use of stronger than room temperature sources.

### 5.1 Test Setup

The test setup for conducting the HADIS tests is shown in Figure 13.

### 5.2 Test Results

The following figures (test results) have been selected from the HADIS digital test data supplied to NASA Langley Research Center and provide a pictorial assessment of the results obtained. A lead selenide, thermo-electrically cooled detector was utilized. See Section 7.0 for additional data.

Figure 14 is a black and white photograph of the color monitor display of a black body point source located just above a propane torch. The spatial images displayed at the left of each of 14 a), b) and c) depict the spectrally integrated spatial scene with an intensity scale provided at the bottom of each scene image. To the right is the spectral distribution of energy in the spatial cell indicated by the cursor. As discussed in Section 4.0, the cursor appears as a white spot in 14 a) and 14 b) because the

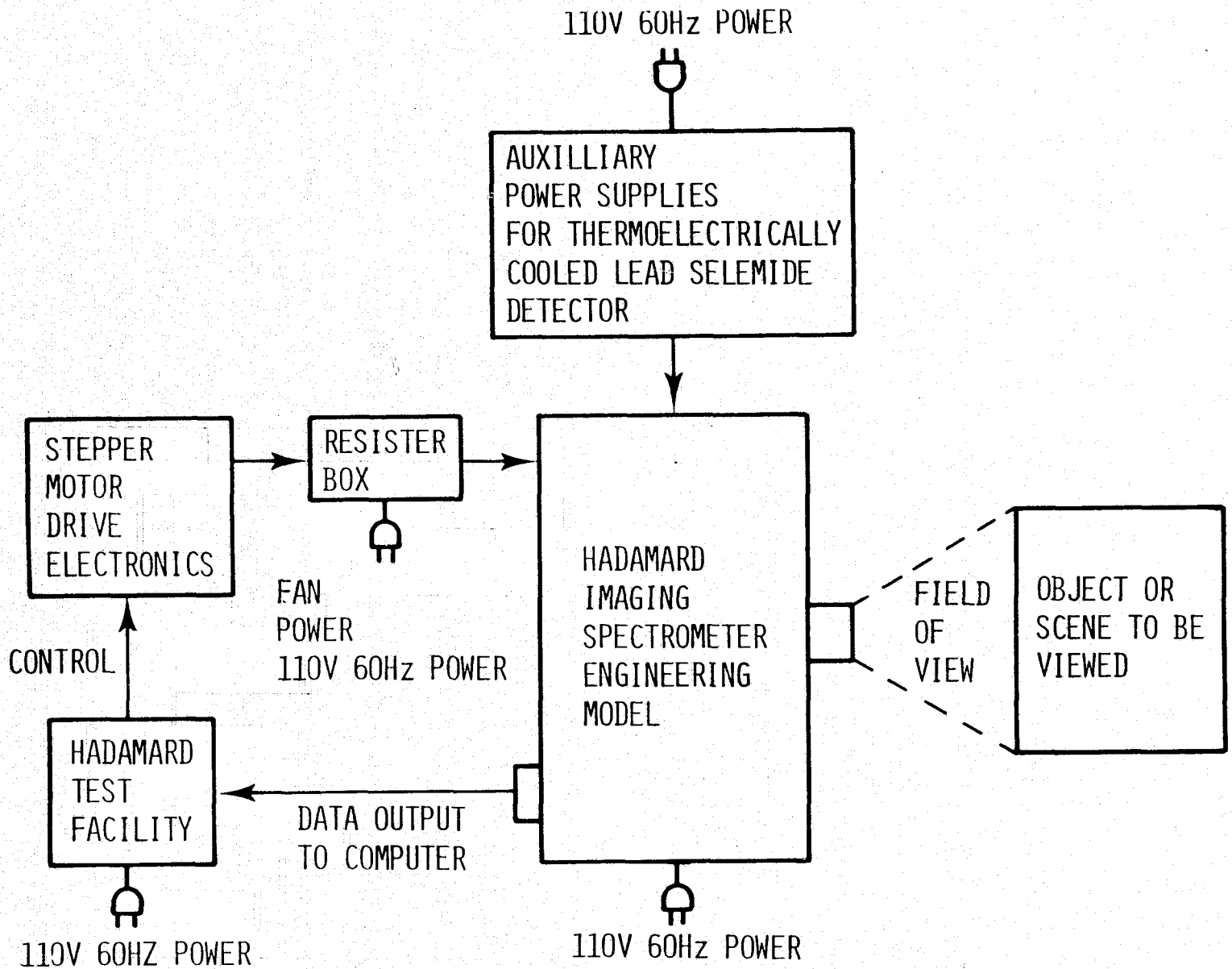


Figure 13. HADIS Test Setup

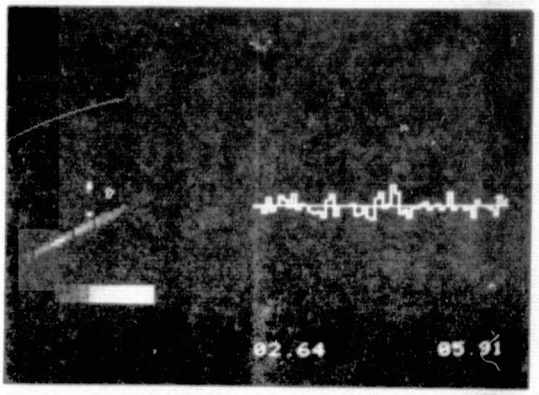


CY-156

a) Background Spectrum

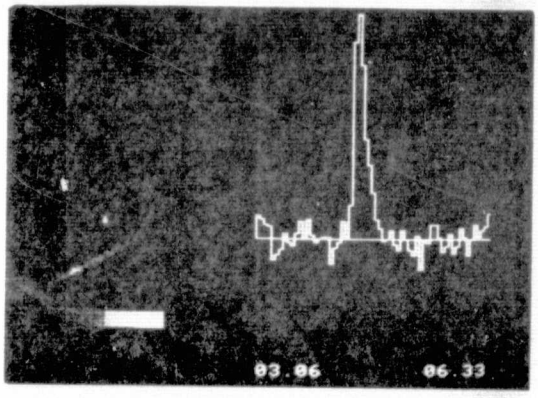


CY-157

b) Flame Spectrum

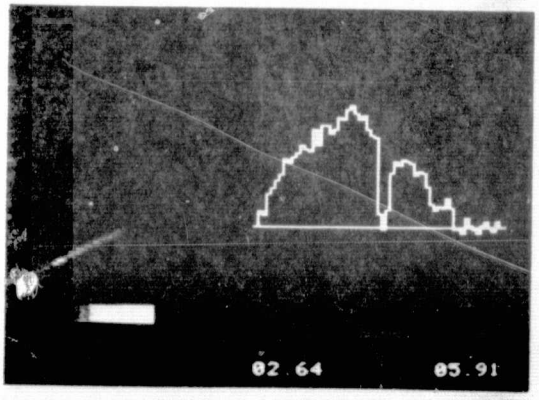


CY-154

c) Black Body Spectrum



Figure 14. 1000° K Black Body Point Source with Propane Torch

integrated intensity of the spatial cell selected is below a preselected level. In 14 c) the cursor appears as a black spot (over black body point source) because the integrated intensity of the selected spatial cell is above the preselected level. In 14 a) the cursor has selected a spatial cell at a point between the black body point source and the flame. The IR spectrum of this selected cell is displayed at the right in microns as abscissa with the ordinate normalized relative to the peak spatial/spectral cell in the entire scene. The displayed spectral data of 14 a) essentially shows background. In 14 b), the cursor has been moved to an arbitrary point on the flame with its corresponding normalized spectrum displayed. The strong $CO_2$ emission at ~4.2 microns is clearly shown.In 14 c), the cursor has been moved to the black body point source, displaying its relative spectrum. In this spectrum the atmospheric $CO_2$ absorption appears as an absorption band at ~4.2 microns. Note for the torch the strong $CO_2$ emission of the flame more than compensated for the absorption observed in 14 c). As shown in 14 a) the black body point source appears brighter than any cell of the flame because it contains more integrated energy under its spectral curve (14 b). than the integrated energy under the flame's spectral curve (14 c). It is noted, however, that the flame has the hottest spatial/spectral cell (peak of 14 b spectrum is higher than peak of 14 c spectrum).

Figure 15 is a black and white photograph of a sequence of 12 spectral images of the scene of Figure 14 and over that portion of the spectrum where the flame rises and drops in spectral intensity.

Figure 16 shows a hot plate with a polystyrene "H" inserted in front of and within the boundary of the hot plate outline. 16 a illustrates the spectrum of a spatial cell in the lower right of the scene and represents background. It is observed that the back-

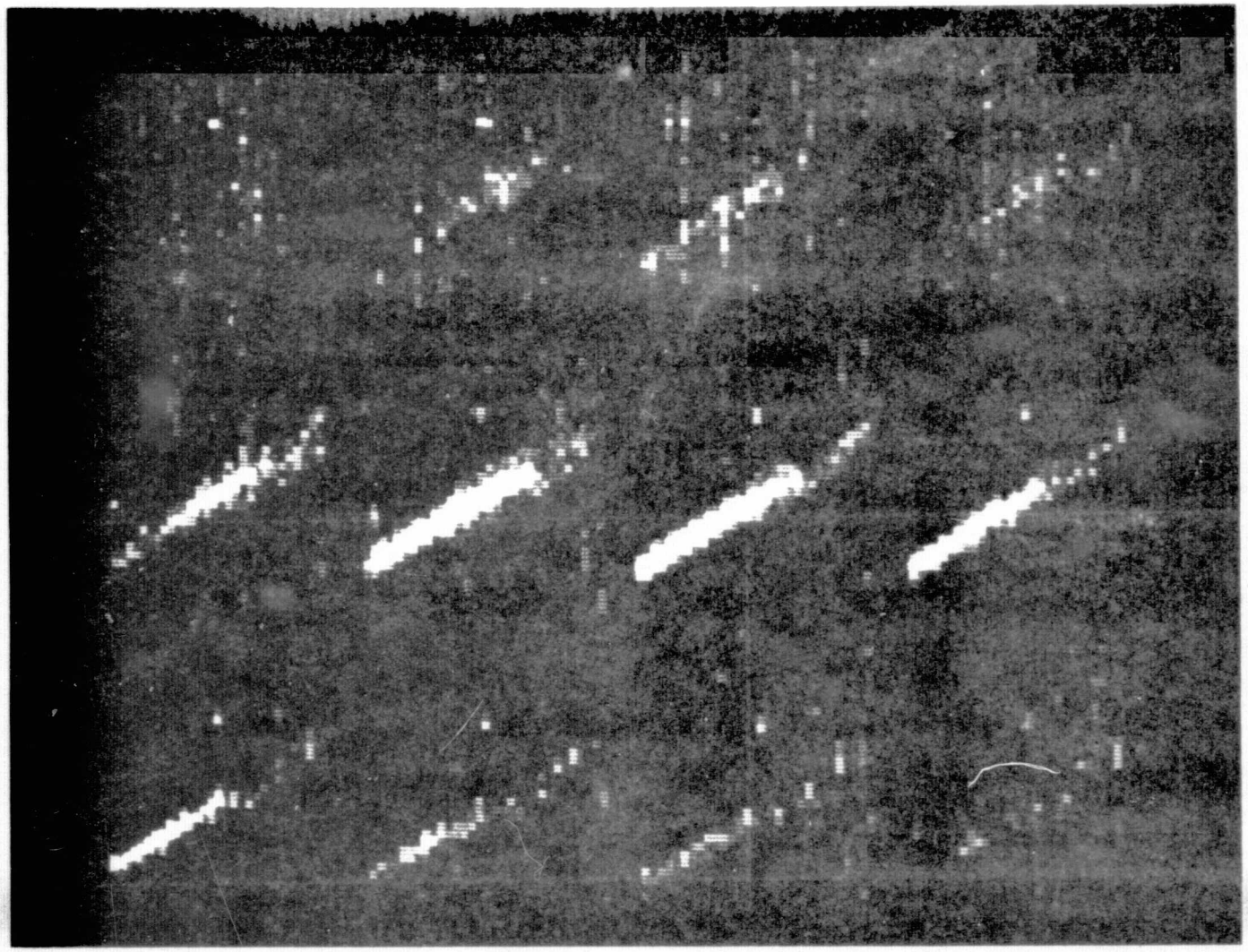

CY-097C

Figure 15. Sequence of Spatial Images of 1000$^{O}$ K Black Body Point Source with Propane Torch

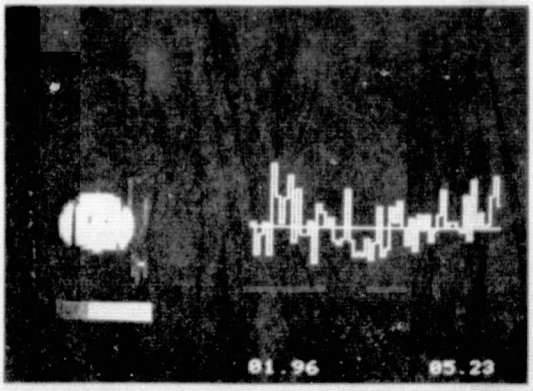


CY-158

a) Background

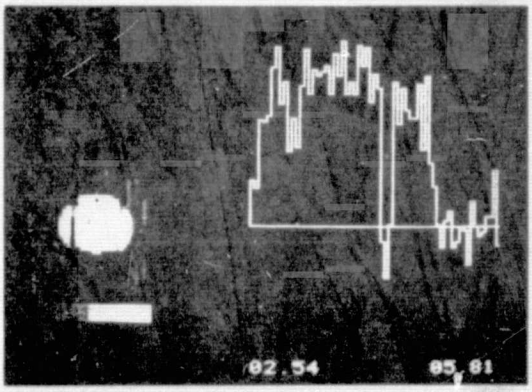


CY-159

b) Hot Plate

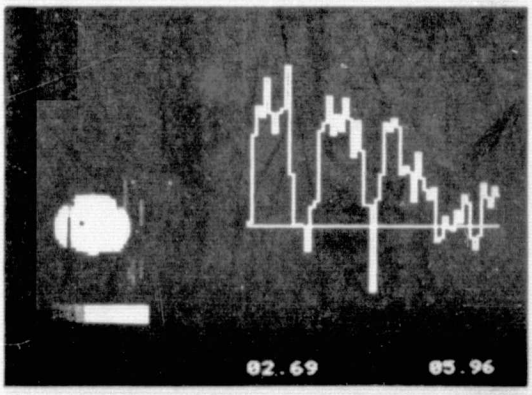


CY-155

c) Hot Plate Through Polystyrene

Figure 16. Polystyrene H Suspended in Front of Hot Plate

ground noise level appears higher than in Figure 14, however it is not. The computer program used, normalizes all intensities to the brightest spatial/spectral cell observed in the scene and sets this point to maximum excursion on the ordinate scale. Since the brightest spatial/spectral cell in this scene had lower intensity than that of the propane torch, the background noise being normalized to the brightest cell, is thus displayed with greater excursions. The spectrum of a point on the hot plate is shown in 16 b) and the spectrum of a point on the hot plate as filtered through the polystyrene is shown in 16 c). Figure 17 illustrates a sequence of 12 spectral images which include the structure of polystyrene absorption bands, i.e., where the polystyrene absorbs, the "H" outline is clearly seen, where it does not, it is not seen.

Additional tests were run to check wavelength calibration. Figure 18 is a display of this test data. 18 a shows a 1000 $^{o}$K black body point source with its spectrum. 18 b illustrates the same source with a polystyrene filter in the optical path. 18 c has a 3-4 micron filter in the optical path, and 18 d illustrates a polyethylene filter in the optical path. By knowing the filter cutoffs and absorption bands one can readily calibrate the system for wavelength.

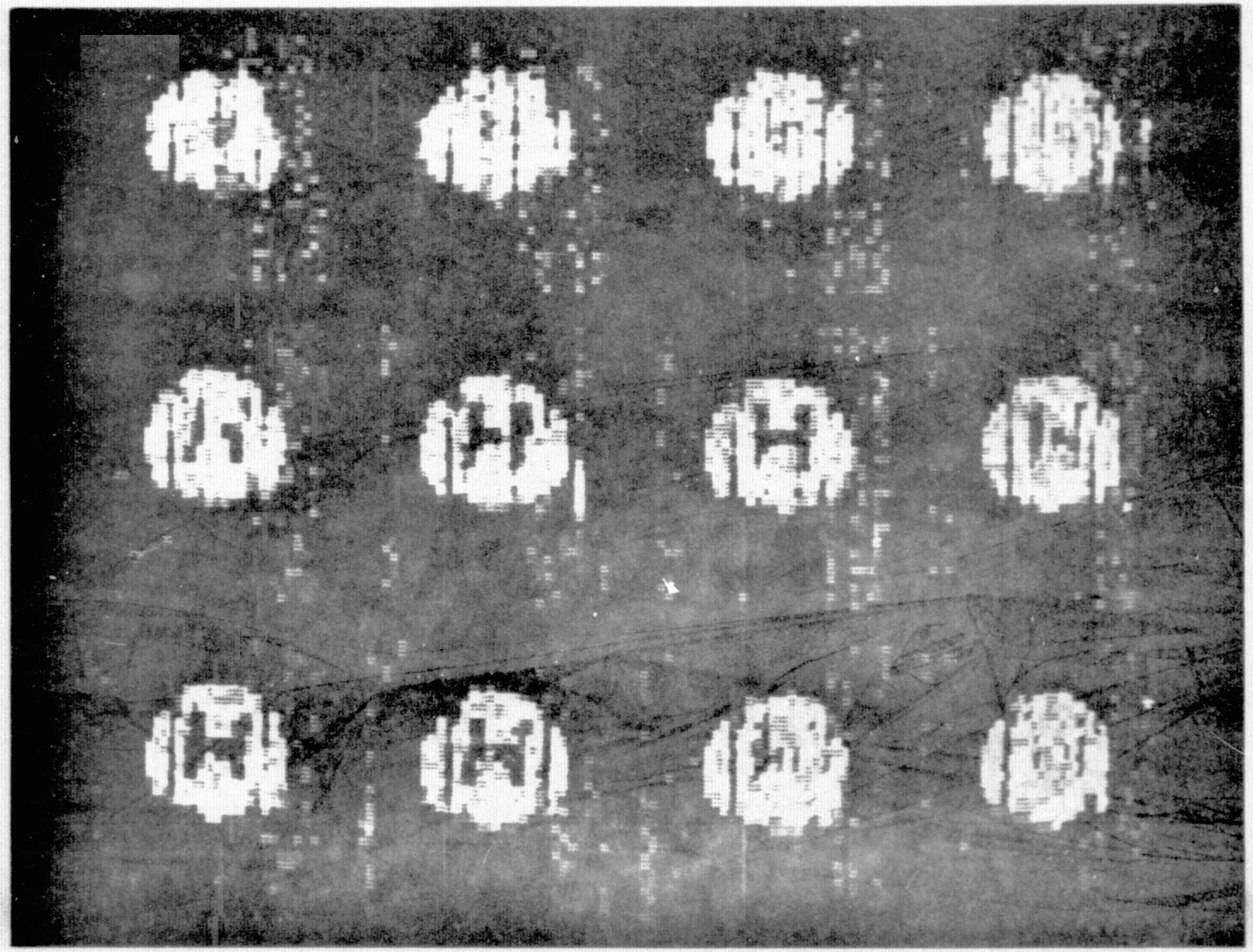

CY-102C

Figure 17. Sequence of 12 Spectral Images of Polystyrene H in Front of Hot Plate

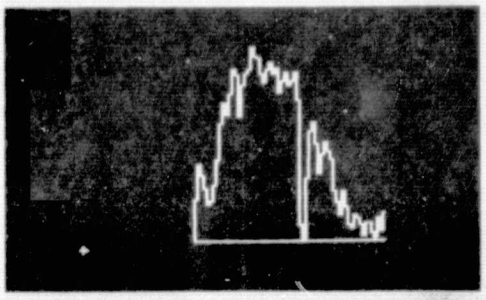

CY-103C

a) Black Body Point Source Spectrum

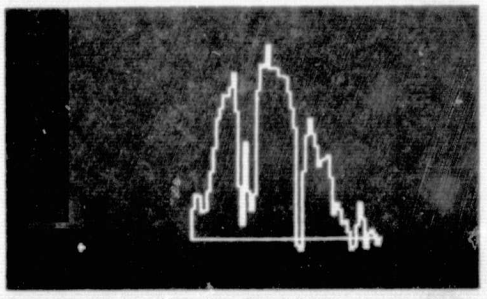

CY-107C

b) a) with Polystyrene Filter

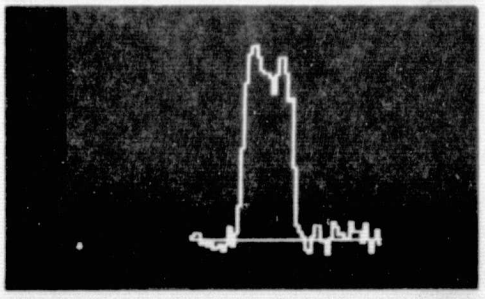

CY-106C

c) a) with 3 - 4 Micron Filter

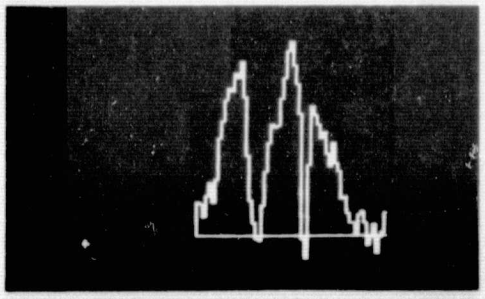

CY-098C

d) a) with Polyethylene Filter

Figure 18. Wavelength Calibration Using 1000° K Black Body Point Source

# 6.0 HADAMARD IMAGER (HADIM) TEST PROGRAM AND RESULTS.

The purpose of the Hadamard Imager Test Program was to verify the mask encoding technique for room temperature scenes. Tests conducted included

a) Point source imaging

b) Extended source imaging

The quantitative results of the HADIM tests are discussed in detail in Section 7.0. In summary the mask encoding technique was successfully demonstrated, however, additional hardware and software requirements resulted from operating at room temperature scenes. Details are given below in Section 6.2. Test results reported below have been selected from the HADIM digital test data provided to NASA Langley Research Center.

## 6.1 Test Setup

The test setup for conducting the HADIM tests is shown in Figure 19.

## 6.2 Test Results

In setting up for operation to view room temperature scenes, it was found that the ripple from the preamp power supply totally swamped the room temperature scene signal. The ripple appeared in the decoded images as alternating strong vertical bands. A special regulator was designed and fabricated. The new regulator reduced the ripple noise to below the signal of the scene. At this point, the instrument sensitivity, although improved, was still well below expectation. The problem was clearly observed by viewing the Hadamard encoded signals for both entrance masks (two separate entrance masks on the entrance encoding wheel). Each mask appeared to have its own

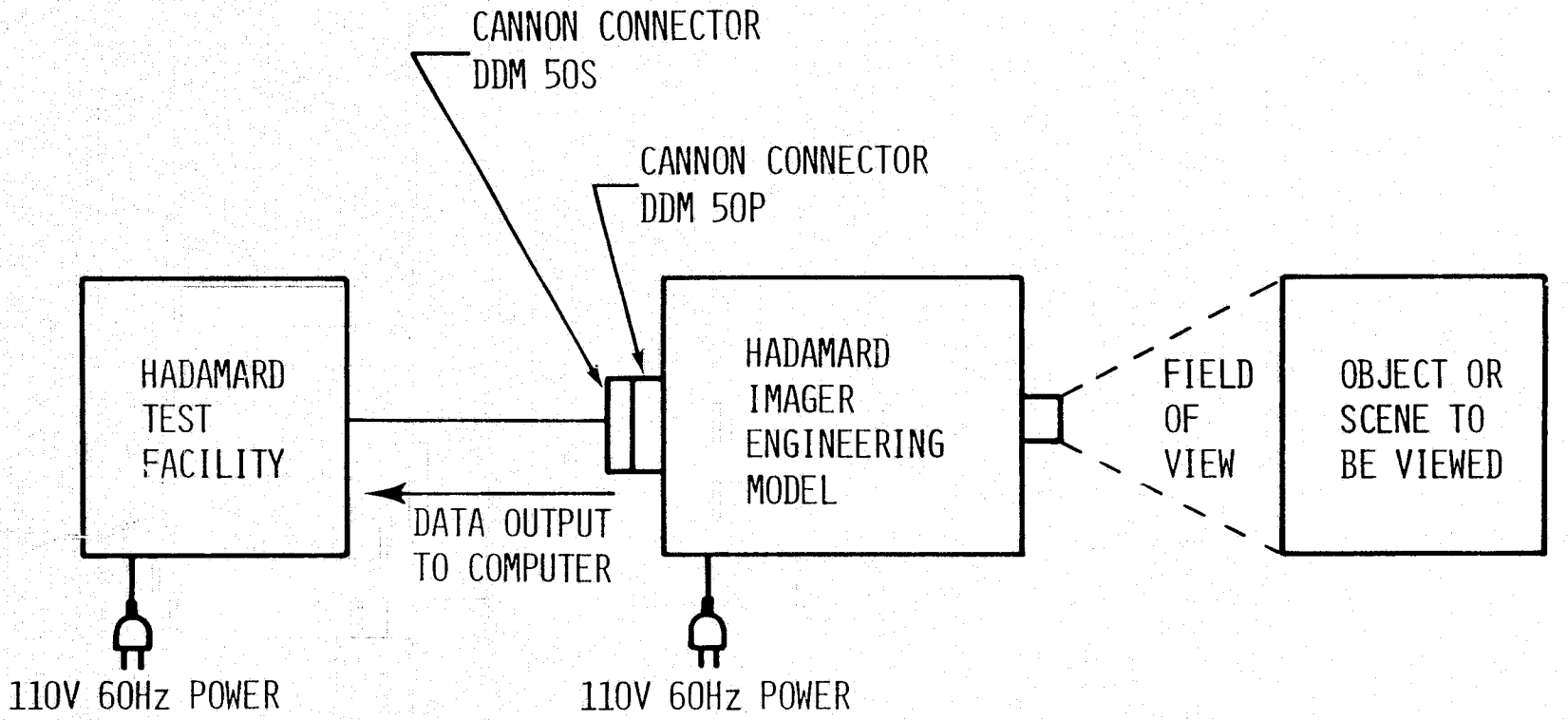


Figure 19. Hadamard Imager Test Setup

characteristic encoded signal sequence independent of normal room temperature scenes. The signal sequence appearance would visually change as one placed a hotter than room temperature object in the field of view. What had happened, was that the liquid nitrogen cooled Hg Cd Te detector was detecting the mask self radiation. The variation in mask radiated IR energy was detected as each mask (with varying emissivity along the mask) rotated past the entrance field stop. Each mask had its own characteristic pattern. To resolve this problem, a computer program was written to store the radiation pattern from each mask and then subtract the mask signal from the room temperature plus mask signal, and then decode. The masks were distinguished by blocking out two (2) of one mask's 1058 status pulses. Hence, one mask had 1058 status pulses, the other 1056. The data which follows is identified as 1056 or 1058 frame data. With the mask signal now subtracted out, the power supply ripple and the detector 1/f noise became the dominant factors. The noise appears as vertical bar structure on the decoded images and is shown in Figure 20. (Scene is black cloth). Figure 20 a) shows one 1058 frame of residual noise after subtracting mask signal. Figure 20 b) shows 11 integrated 1058 frames. The frame RMS noise for Figure 20 a) was 0.532 and that for Figure 20 b) was .144. In comparing 20 a) with 20 b) the 1/f randomness in setting vertical structure is clear. Note: when power supply ripple had dominated, the vertical structure was totally repeatable. (Masks are synchronously driven). It should also be pointed out that the display program normalizes the data so that the strongest cell in the scene appears as white.

Figure 21 is a sequence of scenes of a 1000$^{o}$K black body point

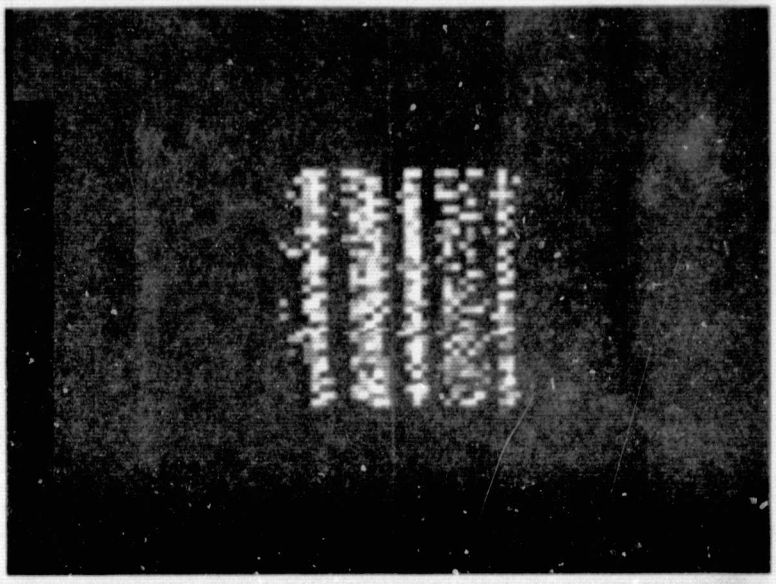

CY-148

a) One 1058 Frame

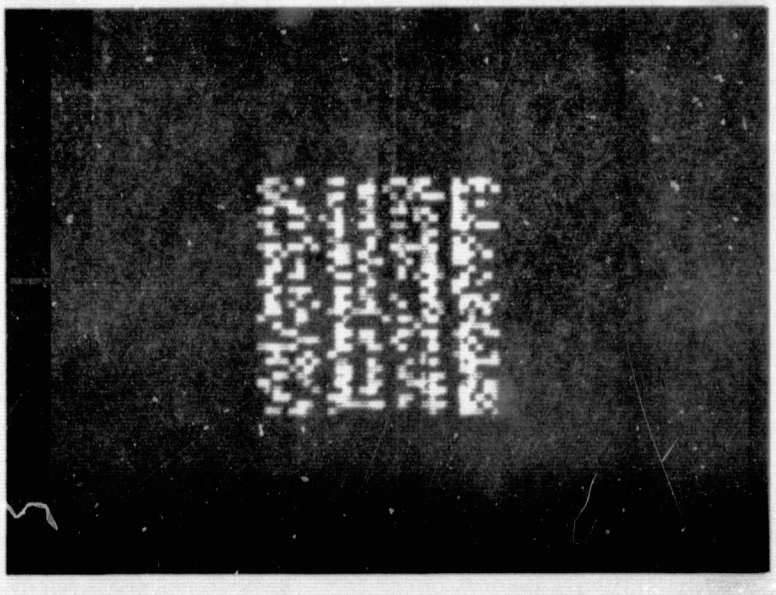

CY-151

b) Eleven Integrated 1058 Frames

Figure 20. Residual Noise After Subtracting Mask Signal, Includes Ripple and 1/f Noise Effect as Vertical Structure

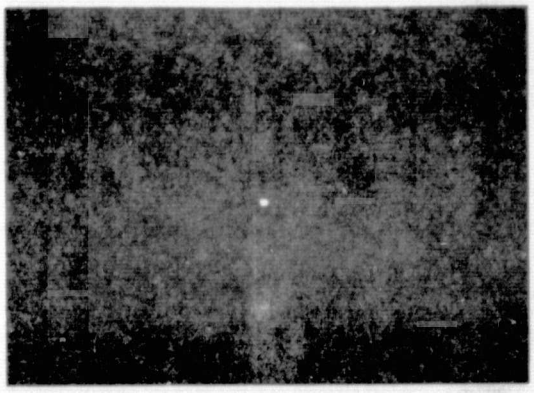

CY-145

a) One 1056 Frame

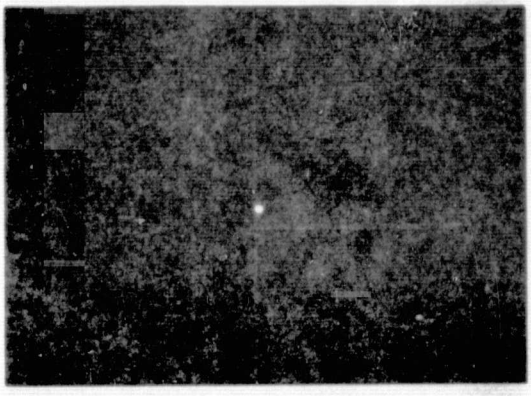

CY-146

b) One 1058 Frame

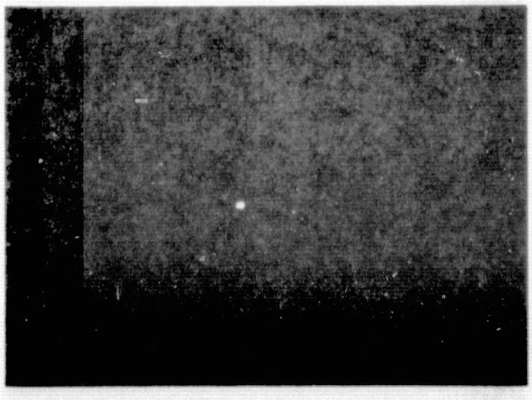

CY-147

c) One 1058 Frame, Point Source Near Left Edge

Figure 21. $1000^{\circ}$ K Black Body Point Source with Mask Signal Subtraction Program

source, using Mask Subtraction Program*. 21 a) shows one 1056 frame of the 1000°K black body point source near center of the field of view. 21 b) shows one 1058 frame of same scene. 21 c shows one 1058 frame of the 1000°K BB point source near the left edge of field of view. Note that the warm cylindrical body of the BB source is observed surrounding the point source location. The darkness immediately adjacent to the point source is caused by the low emissivity plate over source aperture.

Figure 22 shows Dr. Rod Swift's left hand. 22 a), is of one 1056 frame, and 22 b) is of sixteen integrated 1056 frames. In 22 b) the temperature difference between the fingers and hand is clearly observed. Also, along the arm from the left are the following; shirt sleeve, bare wrist, wrist watch, and then hand.

Figure 23 shows Dr. Swift's left hand pressing down on a low temperature BB point source (35° C). 23 a) shows one 1058 frame with the thumb grasping the BB housing on the opposite side from the fingers. 23 b) shows eleven integrated 1058 frames of the same scene except the thumb is placed adjacent to the fingers while pressing down. The effect of 1/f noise is clearly visible in 23 a).

* Mask subtraction program involves covering field of view with room temperature black diffuse cloth and storing mask signal for 1056 and 1058 frames. Cloth then removed, scene plus mask signal taken, appropriate stored mask signal subtracted, then scene signal Hadamard decoded and displayed.

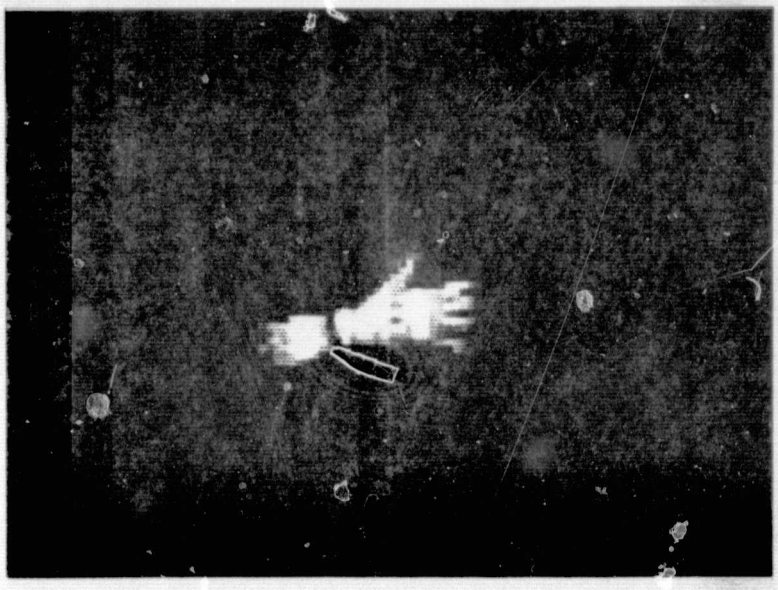

CY-149

a) One 1056 Frame

CY-150

b) Sixteen Integrated 1056 Frames

Figure 22. Dr. Rod Swift's Left Hand

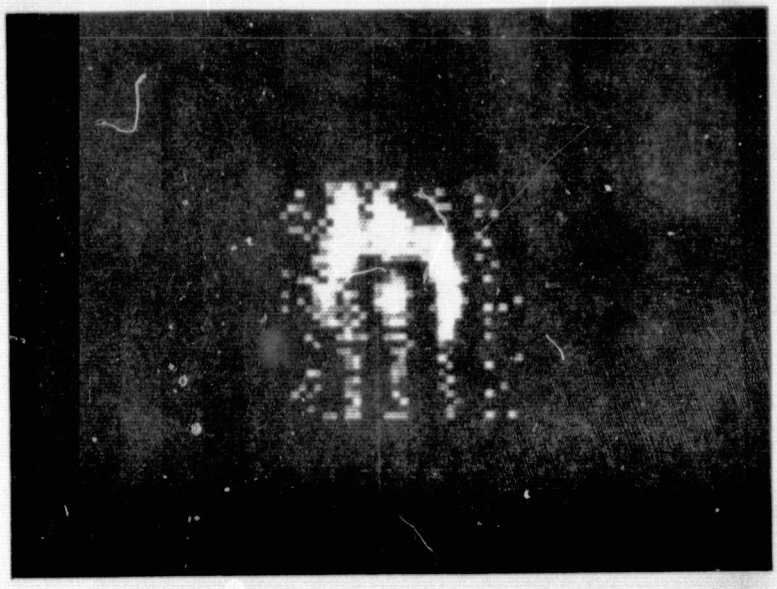

CY-152

a) One 1058 Frame, Thumb Opposite Fingers

CY-153

b) Eleven Integrated 1058 Frames, Thumb Along Fingers

Figure 23. Dr. Swift's Left Hand Pressing Down on a Low Temperature Black Body Point Source (35°C)

## 7.0 SIGNAL-TO-NOISE ANALYSIS

One of the principal advantages to be gained by multiplexing of data is the ability to effectively suppress certain types of noise. A S/N improvement that may be obtained in this way, i.e., the multiplex advantage or Fellgett's advantage, may be utilized in a number of ways. For example, it may be traded off for higher sensitivity, higher resolution, or shorter frame time (higher bandwidth); alternatively, it may be used to reduce performance requirements of the system, such as replacing a cryogenically cooled detector by a radiatively cooled one, or decreasing the size and weight of an optical system.

In this section, we first present a discussion of some of the theoretical implications of various types of noise sources, and how they are affected by the signal multiplexing brought about by the Hadamard transform encoding. We then analyze the results of sensitivity measurements performed with the HADIS and HADIM. Finally, we discuss the BLIP (background limited infrared photodetector) limit as it applies to the use of an instrument such as the HADIM for thermal imaging purposes.

### 7.1 Theoretical Considerations

A question that frequently arises concerns the uses to which a spectrometric imager or other encoding optical instrument can be put in actual practice. The analyses carried out in the past[4, 5, 6, 8, 11] have largely dealt with detector noise limited optical systems, and the detectors have been assumed to have noise figures independent of detector size. While that property does characterize some classes of detectors, other devices show an increase in noise with increasing area -- and that may make multiplexing unfruitful. Harwit and Decker[20] have reviewed some of these sources of noise

for spectrometers. Here we will review these and two additional noise sources, and show how the advantages or disadvantages scale for the two kinds of instruments covered in this report: imagers having n spatial elements, and spectrometric imagers having n spatial and m spectral elements.

We consider the following sources of noise:

$N_1$: Photon noise from the source of radiation. This is the irreducible noise in the incident beam; it cannot be eliminated without eliminating portions of the radiation to be analyzed. We assume here that this noise scales as the square root of the incident number of photons. That means that Bose-Einstein statistical effects which can become significant at very long wavelengths and in high intensity beams are neglected.

$N_2$: Photon noise in the field of view other than from the source to be analyzed. This type of noise is prevalent when the entrance aperture of the instrument is large compared to the source size. Foreground sky radiation, for example, may then constitute a major noise source. However, photon noise from atmospheric emission along the path to the source may remain dominant even when the instrument's entrance aperture is matched to the source size. That is the case we have in mind here.

$N_3$: Occasionally atmospheric transmission may vary between source and detector, so that the source viewed is effectively modulated by more or less random atmospheric effects. This type of noise is frequently encountered in astronomical observations under marginal observing conditions. If the change in transmission is more or less uniform over the entire field of view, and has no marked spectral features, then a total radiation detector can be used in conjunction with the encoded optical instrument, and

most of the effects of $N_3$ can be removed through judicious normalization.

$N_4$: Besides changing the transmission, the atmosphere can also change its emissivity along the light path from the source. This type of noise can also be minimized by careful "chopping" between the field of view containing the source and an immediately adjacent field of view in the sky.

$N_5$: Here the prime source of noise is detector noise from a size-independent detector, or amplifier noise. In practice this condition is frequently found for cold far infrared detectors kept in a cooled cavity behind a cooled filter. The detector resistance may then produce a high noise, or, if the detector noise is very low, pre-amplifier noise may dominate.

$N_6$: Size dependent noise. Here we only treat the D* detectors which exhibit noise proportional to the square root of the detector area.

$N_7$: Some detectors are very slow and effectively attenuate rapidly varying signals. For such detectors rapid scanning, for example, is out of the question, because the system gain would have to be increased to the point where amplifier noise would tend to become dominant in the absence of other noise sources. For such detectors only the minimum number of measurements nm can be contemplated, where n is the number of spectral elements to be resolved and m is the number of spatial elements.

$N_8$: Sometimes the minimum available detector size is much larger than the finest resolution element of available masks. To make optimum use of the sensitive detector area, encoding may then be indicated.

$N_9$: When a detector is kept in a housing that radiates at wavelengths to which the detector is sensitive, the detector may be more strongly limited by this source of noise than by any other. When possible the housing should then be cooled, but in some applications that choice may not be available, and this type of photon noise will then dominate.

Table 5 gives the author's interpretation of the scaling of these different noise sources as a function of n and m.

Table 5

Signal-to-Noise Ratio Gain Relative to Single Element Scanning for n Spectral and m Spatial Elements*

| Noise | Imager | Spectrometric Imager |
|---|---|---|
| $N_1$, $N_2$ | $1/\sqrt{2}$ | 1/2 |
| $N_3$, $N_4$ | Depends on ability to compensate noise by means of reference beam. | |
| $N_5$, $N_7$ | $\sqrt{m}/2$ | $\sqrt{nm}/4$ |
| $N_6$, $N_9$ | 1/2 | $\sqrt{n}/4$ |
| $N_8$** | $\sqrt{m'}/2$ | $\sqrt{nm'}/4$ |

*Assumes de-dispersion for all spectral instruments, and that the optical systems are theoretically optimized or equivalent in all cases.

**For minimum available detector size $N_8$ acts like $N_5$, $N_7$ if n and m are interpreted to represent the number of mask elements imaged onto the minimum size detector. If the detector is larger than minimum size, and falls into the $N_6$, $N_9$ class, $N_8$ will scale like $N_6$, $N_9$ to the point where the minimum detector size is reached, and like $N_5$, $N_7$, beyond. Either way, if m' is the number of spatial elements that could be imaged onto the minimum size detector, the noise scales as shown in the table.

## 7.2 S/N Measurements and Analysis

The results of the test programs described in Sections 5 and 6 of this report effectively presented the qualitative performance of the two implementations of the Hadamard transform technique. However, those results do not in themselves demonstrate that a multiplex advantage was actually achieved. Quantitative measurements are necessary for that purpose, and are essential for a complete evaluation.

Signal-to-noise measurements were made for both instruments under known conditions, including geometry, frame time and numbers of frames of integration, and where a calibrated blackbody was used as a radiation source. In addition, relative observations were made of the S/N improvement achieved by the HADIS for scenes of different spectral content. We now turn to a presentation of these measurements, show how they are in agreement with the expected performance, and discuss their implications in comparison with what might be expected by other techniques.

### 7.2.1 HADIS S/N Evaluation

Experimental setup and operating conditions:

Figure 24 shows the experimental setup. The pertinent parameters and operating conditions are as follows:

1) Blackbody temperature = $1223^{\circ}K$ ($950^{\circ}C$)
2) Blackbody aperture = $0.1\ cm^2$
3) Blackbody range = 200 cm
4) (a) entrance pupil (see 10a, below) = $.130\ cm^2$
   (b) entrance pupil (see 10b, below) = $.189\ cm^2$
5) Rotation speed = 20 RPM
6) Integration time $\simeq 0.9$ msec

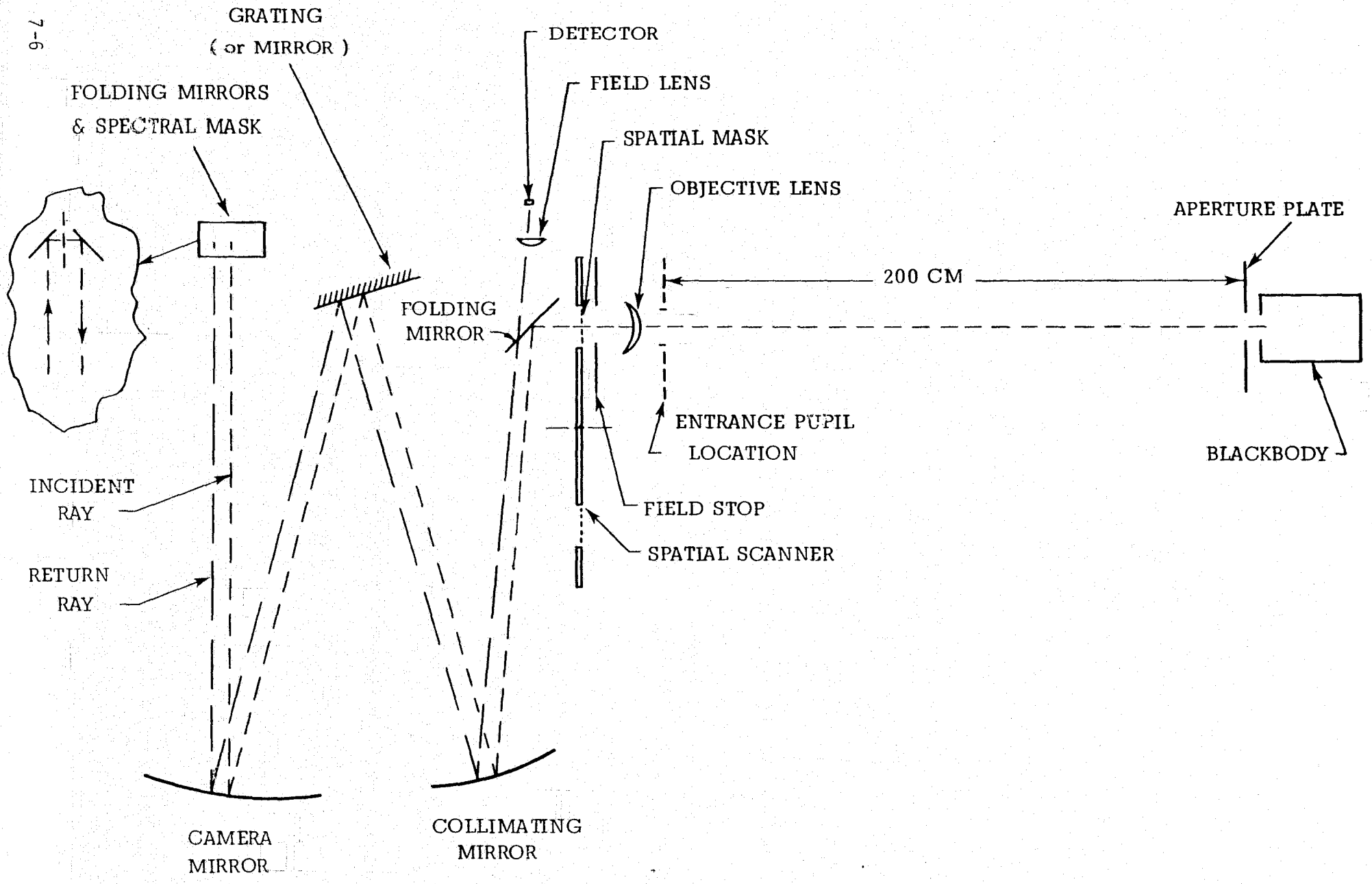


Figure 24 Experimental Setup for HADIS S/N Measurements

7) Bandwidth (1/2T) $\simeq$600 Hz

8) Detector area = .01cm$^2$ (pyroelectric detector)

9) Detector D* $\simeq 1 \times 10^8$ cm Hz$^{1/2}$ w$^{-1}$ (pyroelectric detector at 600 Hz)

10) (a) mirror in grating mount, area = 54 mm x 54 mm

(b) grating, 20 groove/mm @ 9$\mu$m, area = 64 mm x 64 mm

11) (a) optical transmission (see 10a)$\simeq$0.06, including

(i) two KRS-5 lenses, 0.5

(ii) nine mirror reflections, 0.5

(iii) entrance mask code, 0.5

(iv) entrance mask support structure, 0.65

(v) vignetting, optical misalignment, etc., 0.75

(b) optical transmission (see 10b)$\simeq$0.018, including

(i) two KRS-5 lenses, 0.5

(ii) nine reflections, 0.5

(iii) dispersion and de-dispersion, 0.7

(iv) entrance mask code, 0.5

(v) entrance mask support structure, 0.65

(vi) exit mask code, 0.5

(vii) order sorter filter transmission, 0.85

(viii) vignetting, optical misalignment, etc., 0.75

12) (a) passband (see 10a)$\simeq$entire blackbody spectrum

(b) passband (see 10b)$\simeq$7.35 $\mu$m - 8.53 $\mu$m

Note that the optical transmission factors above include the mask code transmission factor of 0.5, and the multiplex advantage is taken herein as the square root of the number of multiplexed elements. In the analysis of Nelson and Fredman[7], the factor 0.5 is included inherently in the computation of the multiplex advantage, and no such code transmission factor would be used. Both analyses yield the same result.

Observed S/N, full spectrum:

This experiment was performed on two separate occasions, with a mirror in the grating mount. Conditions were nominally the same in both cases. Blackbody range may have differed by as much as

4 or 5 cm, but the greatest difference was probably due to optical misalignment or vignetting factors. RMS noise was obtained by obscuring the HADIS field of view and integrating many frames. It scaled in proportion to the square root of the number of frames as would be expected.

$$\text{Signal} = \begin{cases} 743, \text{ first experiment} \\ 650, \text{ second experiment} \end{cases}$$

$$\text{Noise} = \pm 12 \text{ (single frame)}$$

$$\therefore \underline{S/N \simeq 58}$$

Observed S/N, dispersed spectrum:

These measurements were background corrected and averaged over many frames. Noise has been given as the single frame value; it decreased as the square root of the number of frames.

$$\text{Signal} \simeq 11$$

$$\text{Noise} \simeq \pm 12 \text{ (single frame)}$$

$$\underline{S/N \simeq 0.9}$$

Computed S/N, full spectrum:

The power incident on the detector is equal to the power incident on the entrance pupil times the optical transmission; for a $1223^{\circ}K$ blackbody, we have

$$S \simeq 4 \text{ w/cm}^2 \text{ ster} \times 0.1 \text{ cm}^2 \times \left[0.13/(200)^2\right] \text{ ster} \times 0.06 \qquad (12)$$

$$S \simeq 7.8 \times 10^{-8} \text{ watts}$$

The detector noise equivalent power can be obtained from its D*, the area of the detector, and the bandwidth:

$$N_D \simeq \frac{.1 \text{ cm} \times (600 \text{ Hz})^{1/2}}{10^8 \text{ cm Hz}^{1/2} \text{ w}^{-1}} \qquad (13)$$

$$N_D \simeq 2.4 \times 10^{-8} \text{ watts}$$

We must apply the multiplex gain to the above values to obtain the expected S/N:

$$(S/N)_{calc.} \simeq \sqrt{1023} \times \frac{S}{N_D} \qquad (14)$$

$$\underline{(S/N)_{calc.} \simeq 104}$$

Calculated S/N, dispersed spectrum:

The power incident on the detector is equal to the optical transmission times the power incident on the entrance pupil within the spectral bandpass of the instrument. The wavelength dial was set for a low frequency limit of 7.35μm. The dispersion of the spectrograph for a 20 groove/mm grating (see eqn 3 and the following discussion) gives a long wavelength limit of 8.53μm. Only about 3% of the energy of a 1223°K blackbody falls within these limits, so we have:

$$S \simeq 0.03 \times 4 \text{ w/cm}^2 \cdot \text{ster} \times 0.1 \text{ cm}^2 \times \left[0.19/(200)^2\right] \text{ ster} \times 0.018 \qquad (15)$$

$$S \simeq 1.0 \times 10^{-9} \text{ watts}$$

The detector noise is as before, and the same multiplex advantage, $\sqrt{1023} = 32$, must be applied. Therefore,

$$\underline{(S/N)_{calc.} \simeq 1.37}$$

Discussion:

The two measured values agree with their calculated counterparts within a factor of two. Uncertainties in the optical transmission factors alone could easily account for the discrepancies. In particular, the vignetting and alignment factor, 0.75, may be optimistic.

Another important factor in the comparison, and one which is difficult to analyze, is the effective $D^*/(\text{bandwidth})^{1/2}$ for the detector. The information bandwidth is as it was used in the calculations, but in effect it should be convolved with the noise spectrum of the detector to yield the true noise equivalent power. The value of $D^*$ used corresponds to the high frequency end of the bandwidth, having poorest noise performance for a pyroelectric detector. Since the information bandwidth does not cut off sharply at 600 Hz, and since the detector performance is deteriorating rapidly at that frequency, it is not unrealistic to use that value.

We note, incidentally, that images produced with the pyroelectric detector exhibited high frequency noise, appearing completely random in the reconstructed scene. Point sources with a S/N much less than 5 are difficult to discern in the image, whereas extended sources can be observed even when their average S/N is about 1, because they are spatially contiguous.

Spectral multiplexing:

Although they used the HADIS instrument, all the S/N measurements and analysis given above was for use in the imaging mode only - hence, the multiplex gain of only 32.

The achievement of the multiplex advantage was also verified spectrally, and served to point out an important and interesting aspect of spectral multiplexing. Consider the taking of a single

spatial frame by the HADIS, but with the optics set up for diffraction, order sorting, etc., in other words, in its normal operating mode. Let us assume that we obtain a single frame spatial S/N = 8 for the scene. Now consider taking a complete spatial/spectral scene with the same source. If the source has a flat, continuous spectrum, the energy which formerly gave a S/N = 8 will now be divided up to yield information about 63 wavelengths, but with an additional multiplex advantage of a factor of 8. Thus, each spectral image, showing the scene for a wavelength resolution element, will have:

$$\left(\frac{S}{N}\right)_{\text{continuum}} = \frac{8}{63} \times \sqrt{63} \simeq 1 \qquad (16)$$

On the other hand, if our original scene was, in fact, monochromatic, then the spatial/spectral frame would result in having all its energy in one spectral image, with the concurrent multiplex gain $\sqrt{63}$, and the observed:

$$\left(\frac{S}{N}\right)_{\text{monochromatic}} = 8 \times \sqrt{63} \simeq 64 \qquad (17)$$

The other 62 spectral images have no signal, of course, and show only noise.

## 7.2.2 HADIM S/N Evaluation

Experimental setup and operating conditions:

A 1000°K blackbody was placed close enough to the HADIM so that its aperture filled several resolution elements. (The S/N for a single resolution element could then be measured and compared to the calculated value for a solid angle equal to the elemental field of view.) The HADIM was operated in its normal mode, and the single and noise determined for the central element of the blackbody image.

Incident power:

The power incident on the detector from within one resolution cell of the mas' is given by the equation:

$$P_{cell} = W_{1000^{\circ}K} \times A \times \Omega_{cell} \times \eta \qquad (18)$$

where $W_{1000^{\circ}K} = \frac{\text{watts}}{\text{cm}^2 \cdot \text{ster}}$ from a 1000°K blackbody

$A$ = entrance pupil area in $\text{cm}^2$

$\Omega_{cell}$ = elemental field-of-view in steradians

$\eta$ = optical efficiency of the HADIM

From a blackbody sliderule, we find (since a blackbody is a Lambertian radiator):

$$W_{1000^{\circ}K} = 1.78 \ \frac{\text{watts/cm}^2}{\text{ster}} \qquad (19)$$

We previously found A from the details of the HADIM optics:

$$A = 6.97 \ \text{cm}^2 \qquad (20)$$

Note that any misalignment or aberrations of the optical system will result in the effective area being smaller.

The incremental solid angle $\Omega_{cell}$ is also calculated from the optics and the mask cell dimensions. The mean size is 0.00678" square, or 0.0297 $mm^2$. The focal length of the objective lens is 38.1 mm, giving,

$$\Omega_{cell} = \frac{0.0297}{(38.1)}2 \text{ ster} = 2.043 \times 10^{-5} \text{ ster} \qquad (21)$$

Optical efficiency includes (1) $(.85)^2$ for two coated Ge lenses, (2) 0.5 for mask code, (3) 0.65 for mask support structure, and (4) an estimated 0.8 for optical vignetting and aberration effects. The germanium immersion lens is <u>not</u> included, since it is part of the detector, and was automatically included in the detector D* measurement.

$$\eta \simeq (.85)^2 \times .5 \times .65 \times .8 \simeq 0.188 \qquad (22)$$

Therefore, the incident power from the blackbody is:

$$\underline{P_{cell} \simeq 4.77 \times 10^{-5} \text{ watts}} \qquad (23)$$

<u>Detector noise:</u>

The detector tests were conducted using an unfiltered 1000°K blackbody radiation source, as were the test measurements in the HADIM system. For this reason, it is appropriate to use $D^*_{BB}$ (1000°K) for the analysis. The manufacturer's measurements yield, at 10 kHz,

$$D^*_{BB} (1000^{\circ}K) = 4.8 \times 10^{9} \text{ cm Hz}^{1/2} \text{ W}^{-1} \qquad (24)$$

The "break point" for these detectors is near 2-3 kHz, and detectivity drops approximately as $f^{-1/2}$ for lower frequencies. At 40 Hz,

therefore, we estimate the value of $D^*_{BB}$ to be down by a factor 0.14. Since the bandwidth used by HADIM ranges from about 40 Hz to 20 kHz, we shall assume a mean degradation of $D^*_{BB}$ by a factor of 0.4, which indicates domination by low frequency noise, as is observed. Then,

$$\overline{D^*_{BB}} \simeq 1.9 \times 10^9 \text{ cm Hz}^{1/2} \text{ W}^{-1} \tag{25}$$

The noise power of the detector is:

$$P_N = \frac{\sqrt{A_D (\Delta f)}}{\overline{D^*_{BB}}} \tag{26}$$

$$= \frac{\sqrt{1 \text{ cm}^2 \times 2 \times 10^4 \text{ Hz}}}{1.9 \times 10^9 \text{ cm Hz}^{1/2} \text{ W}^{-1}}$$

$$\underline{P_N = 0.74 \times 10^{-7} \text{ watts}} \tag{27}$$

Calculated S/N:

Applying the multiplex advantage to the above values, we then have,

$$(S/N)_{calc} = \frac{P_{cell}}{P_N} \sqrt{1023} \tag{28}$$

$$\underline{(S/N)_{calc} \simeq 20,500}$$

Measured S/N for 1000°K BB:

From the data log book, we have the 1000°K blackbody signal of 97.5 in the fourth attenuator position. At 10 DB per attenuator position, this corresponds to 975 in the second attenuator position (linearity of the attenuator was checked). This signal represents

the total blackbody signal with a room temperature (300°K) "black cloth" scene subtracted off. Using the blackbody sliderule and estimating an emissivity of 0.9 for the cloth, we find the error to be about 0.7% of the true blackbody signal. Making this correction, we have:

$$S \simeq 982 \tag{29}$$

The observed RMS noise for the second attenuator position, again from the log book and taken for one frame, is:

$$N \simeq 0.33 \tag{30}$$

Therefore, the measured S/N is:

$$(S/N)_{meas} = 2975 \tag{31}$$

Discussion and Analysis:

Comparing the measured and calculated values, we find we are achieving a multiplex advantage of only 4.64.* A possible explanation for not having achieved the full multiplex advantage is that the HADIM has become BLIP limited. This limitation is discussed in more detail in Section 7.3.

The minimum resolvable temperature difference at 300°K may be estimated. The power from a 300°K blackbody (including all wavelengths) is about 0.8% of the power from a 1000°K blackbody, and would therefore give,

$$(S/N)_{300^\circ K} \simeq 0.008 \times 2975 \tag{32}$$

$$(S/N)_{300^\circ K} \simeq 23.8$$

But the minimum resolvable temperature difference would correspond to a S/N~1 (for extended sources), so we must see what $\Delta T$ satisfies the equation,

* Testing of the HADIM at NASA Langley, subsequent to preparation of the original manuscript of this report, indicates that drumhead vibration of the encoding masks may be introducing noise three times in excess of that due to the detector. This, or similar sources of extraneous noise, would account for an apparent loss in multiplex advantage, and a multiplex gain of ~15 or higher may actually have been achieved. [22]

$$(300^{\circ}K)^4 \times \left(1 + \frac{1}{23.8}\right) = (300^{\circ}K + \Delta T)^4 \qquad (33)$$

which is based on the total power radiated by a blackbody being proportional to $T^4$. Solving, we have $\Delta T \simeq 3^{\circ}K$.

As is well known, raster scanning thermal imagers achieve much better temperature and spatial resolution, even though their optical speeds and frame times are comparable. It is important to understand why this is so, since the answer gives insight into the areas of application where a S/N gain can truly be realized by Hadamard transform multiplexed imaging. Contributing reasons for the relatively lower performance of the HADIM are:

(1) The HADIM achieved a multiplex gain of only 4.64*, compared to a potential improvement of 32.

(2) Hadamard multiplexed imaging requires that the full field be imaged onto the detector simultaneously. Consequently, the detector must have (in this case) 1023 times the area of a raster-scanned detector; if it is a D* detector (area dependent noise), the potential multiplex gain must be completely traded off to compensate for increased noise.

(3) At the same time, the mask code and support structure introduce optical losses of 0.5 x 0.65 = 0.33.

(4) Raster scanners are able to use small, top-quality, photovoltaic detectors, which have excellent D* value to start with.

* Refer to footnote on preceeding page.

It is interesting to compute what minimum resolvable temperature might have been achieved had these limitations not been imposed. We would have improvement factors of $32/4.64 = 6.9$ in multiplexing, $32/4 = 8$ in (effectively) reduced area size, and perhaps a factor of 2 in initial detector performance. Applying these factors to equation (32), we would then have,

$$(S/N)_{300^{\circ}K} \simeq 2628 \qquad (34)$$

Repeating the calculation of $\Delta T$, with this value substituted in equation (33), we find $\Delta T \simeq 0.03^{\circ}K$. Alternatively, could the encoding mask be fabricated, we could achieve 100 times the number of spatial elements with a $\Delta T \simeq 0.3^{\circ}K$.

## 7.3 The BLIP Limit

As can be seen by reviewing Table 5, there is no net reduction of noise of types $N_1$ and $N_2$, ie., photon statistical noise, brought about by the multiplexing process. The BLIP limit is simply the level at which the $N_2$ type photon noise (usually considered for a $300^{\circ}K$ thermal background) dominates. It represents the limiting performance of a detector, and multiplexing cannot result in a detector achieving a better overall noise performance. (This is not to say that re-distribution of the noise in a scene is not brought about by multiplexing, which may result in improved S/N for regions of higher signal at the expense of S/N for other regions).

There is a further consideration: if the effective quantum efficiency of the detector (including the transmission of its optics) is less than 100%, then the photon signal and its statistical noise must be replaced by the <u>detected</u> photon signal and its statistical noise. The signal is reduced by the quantum efficiency Q; the photon noise is reduced by $\sqrt{Q}$. This has the effect of reducing the BLIP limit by $\sqrt{Q}$.

It is interesting to see if the multiplex gain of 4.64 achieved by the HADIM is consistant with its (Hg, Cd) Te detector having become BLIP limited. We assume that the detector response is limited to 8-14μm, for which we can take the mean spectral D* of the detector to be about $D^*_{\lambda p}/2$. The measured value of $D^*_{\lambda p}$ was given to be $1.7 \times 10^{10}$ for the immersed detector. However, this includes a factor of 4 (theoretical) improvement due to immersion in germanium, so the true $D^*_{\lambda p}$ of the (Hg, Cd) Te chip should be a factor of 4 lower. We need also apply a degradation due to the low frequency operation; we use the same factor 0.4 as before. Then,

$$\overline{D^*} \simeq D^*_{\lambda p}/2 \times \frac{.4}{4} \tag{35}$$

$$\overline{D^*} \simeq 0.85 \times 10^9 \text{ cm Hz}^{1/2} \text{ W}^{-1}$$

Applying the multiplex factor of 4.64 to this figure, we are actually achieving an effective D* in the vicinity of,

$$D^*_{eff} \simeq 3.9 \times 10^9 \text{ cm Hz}^{1/2} \text{ W}^{-1} \tag{36}$$

But the theoretical BLIP limit for the 8-14μm region is relatively flat at about $3 \times 10^{10}$ cm $\text{Hz}^{1/2}$ $\text{W}^{-1}$, which means we are a factor of 7.6 too low. However, the theoretical BLIP limit should be reduced by an amount proportional to the square root of the detector efficiency, which includes the quantum efficiency of the chip and the optical efficiency of the immersion process.

We can make a crude estimate of the optical efficiency from the detector's voltage responsivity before and after immersion. The voltage responsivity can be shown, on theoretical grounds, to be proportional to the product of the bias current and the square of the detector resistance, where the proportionality constant includes the optical efficiency:

$$r_v = K\ R^2 B \tag{37}$$

$$K = \frac{r_v}{R^2 B} \tag{37a}$$

We can then estimate the optical efficiency by ratioing K' and K, where the prime refers to post-immersion:

$$E_{opt} \simeq \frac{K'}{K} = \frac{r'_v\ R^2 B}{r_v\ R'^2 B'} \tag{38}$$

From the detector data: $r_v = 110$, $r'_v = 46$, $R = 68$, $R' = 39$, $B = 20$, and $B' = 56$. Therefore,

$$E_{opt} \simeq 0.45 \tag{39}$$

Typical HgCdTe detectors may be expected to have a quantum efficiency from 20% to 40%. We shall take,

$$QE \simeq 0.25 \tag{40}$$

Then,

$$E = QE \cdot E_{opt} = 0.11 \tag{41}$$

$$\sqrt{E} = .34 \tag{42}$$

and the BLIP limit must be reduced to,

$$D^*_{BLIP} \simeq 1 \times 10^{10} \tag{43}$$

This is about a factor of 2.5 from the $D^*_{eff} = 3.9 \times 10^9$ of equation (36), and indicates that we should have achieved a multiplex gain of 12 (but not the full 32). A multiplex gain of 4.64 is not outside the uncertainties entering into the above calculations.

Clearly the above discussion involves much conjecture, and no real conclusions can be drawn. Ultimately, the BLIP limit becomes the real bound on the system performance, and may be a contributing cause in the case of the present HADIM. The BLIP limit, as applied to a Hadamard multiplexed imager or spectral imager, could be better tested by using an un-immersed, photovoltaic detector with high D*, preceeded by a narrow spectral band filter.

# 8.0 CONCLUSIONS AND DISCUSSION

In this report, we have presented the instrumental development, testing and analysis of a technique to multiplex spatial and/or spectral information by the use of binary optical masks based on Hadamard transforms. Two such instruments were developed, one for simple spatial multiplexing of a 31 x 33 element field, the other for simultaneous multiplexing of a 31 x 33 spatial field and a 63 channel spectrum in the infrared. Besides the instrumental development, the hardware and software were developed to process the data and display it in various forms.

The spectrometric imager, or Hadamard transform imaging spectrometer (HADIS) consisted of a commercially available grating spectrograph, with a spatial encoding mask placed at its entrance focal plane, a spectral encoding mask placed at its exit focal plane, and suitable objective and detector optics. The encoded radiation was de-dispersed and condensed onto detectors of various types: a pyroelectric detector for the entire IR spectrum to 25$\mu$m, and a PbSe detector for the 2-5$\mu$m band. It was tested by obtaining and decoding point source and extended images in various areas of its field of view, and by obtaining and decoding spatial/spectral data for both point and extended images with various types of spectral characteristics. These data and images were presented in Section 5.

The fact that a multiplex advantage was gained was verified experimentally, by careful signal to noise measurements which were compared to analytic estimates. The calculated and measured values agreed to well within a factor of two (for spatial only images), where the calculation included the theoretical multiplex advantage of 32 for the 1023 element spatial field. (The reduction of the true multiplex advantage due to the mask code was treated as an optical loss.) A spectral multiplex advantage, a factor of 8, was also verified.

The sensitivity of the HADIS was shown, in the analysis of its design, to have two basic limitations: the small size of its entrance pupil, which is related to the optical speed of the spectrograph and the size of its diffraction grating; and the comparatively large detector size required to fill the exit pupil. There are applications, however, where these limitations cease to be of importance. For example, as a telescopic focal plane device having a higher f/number than the HADIS (f/7), the telescope would become the limiting optical element. With regard to the detector, its size is of no importance if its noise is size independent; this is the case with some kinds of detectors.

In regard to the detector size, it should be emphasized that spectroscopic multiplexing can always achieve a S/N advantage over a non-multiplexed system, since the ability to reverse-pass the encoded radiation off the grating and thereby de-disperse it means that no larger a detector needs to be used.

The Hadamard transform imager (HADIM) consisted of the spatial encoding subassembly of the HADIS, but used with a faster optical system and a high performance, cooled (Hg, Cd) Te photoconductive detector. It was tested by imaging various thermal sources, both point and extended, in various parts of its field of view. Examples of these images were presented in Section 6.

Careful signal to noise measurements were also done for the HADIM, and compared to computed values in order to establish the extent to which a multiplex advantage was achieved. Although it has a potential multiplex gain of 32, a gain less than 5 was all that could be achieved with the (Hg, Cd) Te detector. A contributing reason may be that, used as a thermal imager with a 300$^{o}$K thermal background or scene, a multiplexed high level detector soon achieves the BLIP limit, where detector noise ceases to be the limit and photon statis-

tical noise (shot noise) becomes dominant.

Furthermore, since there is no spatial equivalent to the de-dispersion process spectrally, the required detector area, compared to an idealized scanning system, must increase proportionally to the number of elemental fields of view. For this reason, if a D* detector is used, i.e., one having a noise generation proportional to the square root of its area, no multiplex gain can be realized.

On the other hand, if the HADIM is used for non-BLIP limited applications, and uses an appropriate, non-area-dependent, detector, it can give a true advantage over competing instruments. Applications are discussed in more detail below.

There are certain systematic signal perturbations to which the Hadamard transform encoding technique is subject. As long as they are repetitive and not scene dependent, they can be removed during the data processing. An example of this type of perturbation is modulation produced in the detector output because of varying reflectivity or emissivity of the spatial encoding masks as they rotate.

Another type of perturbing effect, which is scene dependent, is mechanical runout of the spatial encoding mask as it rotates. This is equivalent to an oscillatory motion of the scene in the field of view during a frame. This runout could have the effect of causing a point source to disappear behind the mask support structure for a portion of the scan. The results of this particular phenomenon have not been analyzed, but they may be the cause of low level "alias" images occasionally observed with point sources.

Other types of mechanical imperfections in the encoding masks, or jitter in the timing or integration time, would be expected to affect the Hadamard transform. Although these affects were not

observed in the test programs for the HADIS and HADIM, they are potential sources of error and are worthy of further analytic and empirical analyses.

A number of applications of Hadamard transform spectrometric imagers (or imagers, where high spectral resolution is not a goal) suggest themselves. There are many others that may be found in the future.

In meteorological studies from satellites, for example, the thermal structure of the atmosphere may be determined across each viewing scene, by obtaining a series of pictures at wavelengths that range from the center of an absorption line out into its wings. Since the atmospheric transmission in the wings is higher, the radiation received by the sensor comes from lower layers in the atmosphere. At the line center on the other hand, the sensor receives radiation only from the topmost region of the absorbing layer.

Spectral studies of this type were carried out as long as a decade ago by Hanel and Wark[21] and by others; but with a spectrometric imager pictorial data could be obtained simultaneously across an entire carbon dioxide absorption band, or possibly even several different abosrption bands. In this way detailed local atmospheric maps showing temperature as a function of height in each locality would be obtained. Observations in the water vapor lines could then also add information about atmospheric humidity as a function of height or temperature.

In astronomy one frequently encounters three dimensional maps that show the distribution of the doppler shift -- or the line of sight velocity -- across an interstellar cloud or nebulosity.

The rotational structure of galaxies is similarly determined. These velocity distributions essentially are maps of intensities in adja-

cent spectral elements. The velocity distribution often is different for differing atomic species, and for different states of ionization of each species. A number of different atomic transitions need therefore be studied and the velocity distribution across the field of view determined for each one separately.

A question then naturally comes up concerning the usefulness of spectrometric imagers if the most commonly used detectors have noise figures that increase with increasing detector size. Table 5 shows that for such detectors -- which scale like $N_6$ -- there is no advantage at all in spatial multiplexing, unless very high spatial resolution is envisaged. In that case situation $N_8$ arises. That is the case where the optical system is capable of very fine imaging, but the lowest noise detectors are not available in sufficiently small sizes. It then is advantageous to use a very finely divided mask to obtain a signal-to-noise ratio advantage through multiplexing.

Masks with structure as fine as 0.1 mm and tolerances 10% of that value are now fairly standard, and there is no reason why somewhat finer masks could not be used in the near infrared with high speed optics. The resolution element of the mask need not be much larger than the diffraction limited size which is of order $f\lambda$, where f is the focal ratio (f/number) of the system and $\lambda$ is the wavelength. At a wavelength of 10 microns an f/3 optical system requires apertues no smaller than 0.03 mm. But that size nevertheless is much smaller than the size of the smallest low noise detector available on the market.

Since such high quality optical systems are currently available, it follows that the most powerful imaging systems should be able to make good use of masks, even when D*-type detectors are to be used.

Many recent applications, however, involve detectors that do not show a D* behavior. Most of the liquid helium cooled photoconductive detectors, for example, fall into that class. Such detectors are now available at least for short duration space flights and could be used in any variety of observing modes.

For the highest quality detector of this type, the main source of noise appears to be preamplifier noise, $N_5$, and Table 5 shows that there is a considerable advantage than in both spatial and spectral encoding; it therefore has advantages in spectrometric imaging.

In many space applications there may also be noise that largely depends on energetic particle impacts on the optical system. Energetic radiation in the ionosphere then is the prime source of noise. This may again mean that we deal with a detector size independent, noise far stronger than the photon noise. Under these conditions an optical system again will show gains through encoding both in the spectral and spatial modes.

A variety of applications therefore await realization. It is true that spectrometric imagers will tend to be most useful in work that requires both high spatial and high spectral resolution. Since an instrument that lends itself to that kind of study has not been available to date, few scientists and engineers have given much thought to potential applications. But it seems unlikely that an instrument capable of supplying substantial increases in information about a complex scene will long remain unused.

REFERENCES


1. M.J.E. Golay, J. Opt. Soc. Amer. 39, 437 (1949) and 41, 468 (1951).
2. R.N. Ibbett, D. Aspinall, and J.F. Grainger, Appl. Opt. 7, 1089 (1968).
3. J.A. Decker, Jr., and M. Harwit, Appl. Opt. 7, 2205 (1968).
4. P. Gottlieb, I.E.E.E. Trans. Inform. Theor. IT-14, 428 (1968).
5. N.J.A. Sloane, T. Fine, P.G. Phillips, and M. Harwit, Appl. Opt. 8, 2103 (1969).
6. J.A. Decker, Jr., Appl. Opt. 10, 510 (1971).
7. E.D. Nelson and M.L. Fredman, J. Opt. Soc. Amer. 60, 1664 (1971).
8. M. Harwit, P.G. Phillips, T. Fine, and N.J.A. Sloane, Appl. Opt. 9, 1149 (1970).
9. M. Harwit, P.G. Phillips, L.W. King and D.A. Briotta, Jr., Appl. Opt. 13, 2669 (1974).
10. P.G. Phillips and M. Harwit, Appl. Opt. 10, 2780 (1971).
11. M. Harwit, Appl. Opt. 10, 1451 (1971).
12. M. Harwit, Appl. Opt. 12, 285 (1973).
13. J.E. Stewart, Infrared Spectroscopy, Marcel Dekker, Inc., New York (1970); this is a generally good reference on IR spectroscopy, including the design of spectrograph optical systems.
14. A.B. Shafer, L.R. Megill, LeA. Droppleman, J. Opt. Soc. Am. 54, 879 (1964).
15. T. Namioka and M. Seya, Science of Light 16, 169 (1967).
16. C.D. Allemand, J. Opt. Soc. Am. 58, 159 (1968).
17. J. Reader, J. Opt. Soc. Am. 59, 1189 (1969).
18. M.V.R.K. Murty, Appl. Opt. 11, 1637 (1972).
19. P. Fellgett, J. Phys. Radium 19, 187 (1958).

REFERENCES (Cont'd)

20. M. Harwit and J.A. Decker, Jr., Reports on Progress in Optics 12, 102 (1974).

21. R.A. Hanel and D.Q. Wark, J. Opt. Soc. Amer. 51, 1394 (1961).

22. D. Jobson, NASA Langley, Private Communication, 21 April 1976